

REPORT DOCUMENTATION PAGE				<i>Form Approved</i> OMB No. 0704-0188	
Public reporting burden for this collection of information is estimated to average 1 hour per response, including the time for reviewing instructions, searching existing data sources, gathering and maintaining the data needed, and completing and reviewing this collection of information. Send comments regarding this burden estimate or any other aspect of this collection of information, including suggestions for reducing this burden to Department of Defense, Washington Headquarters Services, Directorate for Information Operations and Reports (0704-0188), 1215 Jefferson Davis Highway, Suite 1204, Arlington, VA 22202-4302. Respondents should be aware that notwithstanding any other provision of law, no person shall be subject to any penalty for failing to comply with a collection of information if it does not display a currently valid OMB control number. PLEASE DO NOT RETURN YOUR FORM TO THE ABOVE ADDRESS.					
1. REPORT DATE (DD-MM-YYYY) 16-10-2010		2. REPORT TYPE Final Report		3. DATES COVERED (From - To) 15-07-2008-14-07-2010	
4. TITLE AND SUBTITLE Flow Control Technology				5a. CONTRACT NUMBER 6419	
				5b. GRANT NUMBER	
				5c. PROGRAM ELEMENT NUMBER	
6. AUTHOR(S) Stefan G. Siegel, Ph.D				5d. PROJECT NUMBER	
				5e. TASK NUMBER	
				5f. WORK UNIT NUMBER	
7. PERFORMING ORGANIZATION NAME(S) AND ADDRESS(ES) Siegel Aerodynamics Inc. 1111 Lavender Way, Pueblo, CO 81001				8. PERFORMING ORGANIZATION REPORT NUMBER	
9. SPONSORING / MONITORING AGENCY NAME(S) AND ADDRESS(ES) US Air Force Academy 2410 Faculty Drive Air Force Academy, CO 80840				10. SPONSOR/MONITOR'S ACRONYM(S) USAFA	
				11. SPONSOR/MONITOR'S REPORT NUMBER(S)	
12. DISTRIBUTION / AVAILABILITY STATEMENT A, Approved for public release, distribution is unlimited					
13. SUPPLEMENTARY NOTES Work was performed under subcontract through Digital Consulting Services					
14. ABSTRACT This report summarizes work performed by Dr. Stefan Siegel at the US Air Force Academy Aeronautics Research Center. While the overall subject of the contract was research in the area of feedback flow control, this report specifically covers work done under funding from the National Science Foundation investigating Ocean Wave Energy Conversion. The particular approach involves use of a Cycloidal Turbine for wave energy conversion, which requires feedback control for successful and efficient operation.					
15. SUBJECT TERMS Feedback Flow Control, Ocean Wave Energy, Cycloidal Turbine					
16. SECURITY CLASSIFICATION OF: unclassified			17. LIMITATION OF ABSTRACT unclassified	18. NUMBER OF PAGES 55	19a. NAME OF RESPONSIBLE PERSON Stefan G. Siegel
a. REPORT unclassified	b. ABSTRACT unclassified	c. THIS PAGE unclassified			19b. TELEPHONE NUMBER (include area code) 719 545 7835

*Final Report for
Employment Agreement # 6419*

Title:

Flow Control Technology

Between

Digital Consulting Service (DCS)

And

Siegel Aerodynamics, Inc.

For work performed by

Dr. Stefan G. Siegel

From

July 2008 to July 2010

Contents

Introduction	3
Scope of this document	3
Introduction to the Project	3
Wave Power Potential	3
State of the art wave power devices	4
Cycloidal Propellers.....	6
Adaptation of a cycloidal propeller to wave power extraction	7
Experimental Work	8
Water Tunnel Cycloidal Propeller Experiments	8
Design goals and objective.....	9
Mechanical setup	9
Electrical and software design	11
Experimental Results	12
Shallow Water Wave Energy conversion	18
Construction of the USAFA Wave Tunnel	31
Cyloidal Wave Energy Converter	31
Simulations.....	32
Numerical Approach	32
Potential Flow Theory	32
Linearized Free Surface Boundary Condition.....	33
Potential Vortex under a Free Surface in Infinite Depth Water	34
Bottom Boundary Condition	34
Potential Vortex under a Free Surface in Finite Depth Water	34
Computational Setup	35
Results Deep Water Simulations.....	35
Resolution Study	36
Single Vortex Simulations	39
Multi-Vortex Simulations	41
Wave Cancelation	43

Results Intermediate Water Simulations	44
Flat Plate Simulations.....	48
Cadet and Faculty / Researcher involvement	51
Conclusions	53
References	53
Publications resulting from this research program	53
Open literature references	54

Introduction

This document summarizes work that was performed at the US Air Force Academy, Department of Aeronautics, Aeronautics Research Center, between July 2008 and July 2010. The work was performed by Dr. Stefan G. Siegel, President, Siegel Aerodynamics, under subcontract to the Air Force Academy through Digital Consulting Service (DCS). The contract was monitored and administered on the Air Force Academy side by Dr. Thomas E. McLaughlin, Director of the Aeronautics Research Center. This report will be available through the Defense Technical Information Center (DTIC) fulfilling the requirement for a final report outlined in the Statement of Objectives.

Scope of this document

The Statement of Objectives specified work to be done in the general area of feedback flow control, while specifically naming two projects that were or are funded through external research grants. The first project, Aero Servo Optics, was funded by the Air Force Office of Scientific Research (AFOSR) as well as the Office of Naval Research (ONR). It was run by Dr. Jürgen Seidel, Ph.D, as the Primary Investigator (PI), and successfully finished in 2010. Dr. Siegel was responsible and performed the experimental setup, data acquisition and experimental post processing software for this project, as well as conducted and / or supervised the experimental measurements. For this project, a separate final report has been submitted by Dr. Seidel and is available through DTIC.

The second project in the Statement of Objectives is Cycloidal Wave Energy Conversion, funded through a three year grant from the National Science Foundation. This project was run by Dr. Stefan G. Siegel as PI, it started in September of 2008 and will finish in September of 2011. Thus, at the writing of this report, the second year of this program has just finished.

To prevent redundancy in the reports submitted to DTIC, it was suggested by the responsible government POC, Dr. Thomas McLaughlin that this report should only cover the work performed for Cycloidal Wave Energy Conversion. The Aero Optics work performed by Dr. Siegel is documented in detail in Dr. Seidel's final report, which is hereby included in its entirety by reference. Thus, the remainder of this document summarizes two years of research into a novel approach to extract energy from ocean waves, a device called a Cycloidal Wave Energy Converter, or CycWEC.

Introduction to the Project

The following sections detail the background of this project, along with the idea behind cycloidal wave energy conversion. They are adapted from the proposal request to NSF.

Wave Power Potential

Among alternative energy sources, wave power is one of the most abundant sources on earth. The World Energy Council [8] has estimated the world wide annual amount of wave power energy at 17.5

PWh (Peta Watt hours = 10^{12} kWh). This is actually comparable to the annual world wide electric energy consumption, which is currently estimated at 16 PWh. Thus, wave power has the potential to provide a large portion of the world's electric energy needs, if it can be tapped in an efficient way. In addition to the energy availability, wave power has some other advantages. Since a large portion of the world's population lives close to the ocean shores, the distance between energy production and consumption is small. This reduces transmission losses and necessary investments into transmission lines. As opposed to other alternative energy sources, like wind, stream and solar energy, the installation of wave power devices does not require use of already precious real estate. This makes wave power an ideal energy source for providing renewable energy in an efficient manner to densely populated coastal areas.

	Solar	Wind	Tidal	Wave
Energy Source	Radiation / Sun	Wind / Air	Water / Tides	Wind / Water
Power Density	1 kW / m ² (at peak solar insulation)	1 kW / m ² (1.5 MW GE windmill at 12 m/s)	5 kW / m ² (3 m/s tidal flow speed)	25 kW / m (San Francisco annual average)
Availability	Poor – clouds, days only	While wind is blowing	Diurnal cycles	Day and night
Predictability	Poor due to clouds and weather	Poor – weather forecast	excellent	good
Prediction Time scales	hours	days	Centuries	Days

Table 1: Comparison of alternative energy sources for providing electric power (adapted from [9])

Table 1 compares some other aspects of different alternative energy sources, most importantly their availability and predictability. In both areas wave power surpasses more traditional alternative energy sources like solar and wind. In addition, the large amount of energy contained in typical water waves is striking, which allows for the construction of relatively small devices that extract a large amount of energy.

State of the art wave power devices

Figure 1 shows schematic sketches for a number of different wave energy conversion devices that have been investigated in the past and some that are currently being developed. A number of commonalities in the designs can be observed. The first is that all devices require a connection to the sea bed in order to extract energy, which has two main drawbacks. First, a seabed connection makes the device vulnerable in heavy seas and storms, in the same way as an anchored ship is vulnerable in a storm (and will likely break the anchor line). Survivability has been a major problem for many wave power devices, with some being destroyed by the elements as early as during deployment [8]. And second, for most of the devices the load imposed onto the seabed connection is proportional to the power which the device can extract. This means that the anchor point needs to be stronger and thus more costly as more energy is being extracted since an underwater foundation is an expensive item to construct. Therefore, many of these devices cannot easily be scaled up to power plant levels of energy extraction. In addition, since the devices need to be anchored to the sea floor, they are not well suited to operation in deep water waves, where the ocean floor may be hundreds of meters away from the surface. However, most wave energy

is contained in deep water waves, and the energy density of a wave decreases as it approaches shallow water. Thus, most devices cannot operate in the most promising locations for wave power extraction.

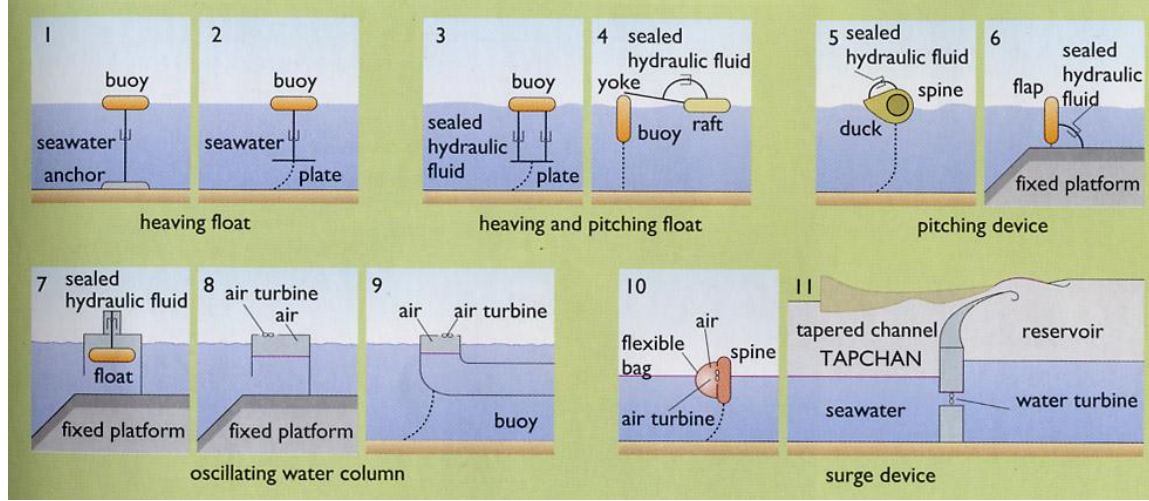


Figure 1: Wave energy converters that have been investigated in the past (from [8])

The second common design feature is that most wave power devices will only extract energy from one component of the wave motion, for example, the buoy devices (Figure 1, designs 1-3) will only extract energy from the vertical motion of the waves. However, in a shallow water wave most energy is contained in flow oscillating in the horizontal direction, while in a deep water wave the energy is evenly split in horizontal and vertical oscillation. This limits a buoy or oscillating water column device to a theoretically optimum energy extraction efficiency of 50%. If the device is small in the third dimension compared to the length of the incoming waves (termed a “Point Absorber”), the efficiency of the buoy or oscillating water column device drops further to 25% at most [10].

From a fluid dynamic perspective, the devices shown in Figure 1 employ two fundamentally different methods to extract energy from the flow. The majority of the devices (1-7) feature an element (typically a buoy) that moves at or below the wave induced flow velocity, with the motion being induced by the drag force imposed onto the element by the flow. In a first order approximation, the instantaneous Power P that can be extracted this way is proportional to the drag force D times the instantaneous velocity V with which the element moves,

$$P \propto D \cdot V . \quad (0.1)$$

The drag force D can be further expanded in terms of the drag coefficient c_D , the velocity V and the area A of the element as well as the fluid density ρ ,

$$D = \frac{1}{2} c_D \rho A V^2 . \quad (0.2)$$

Thus, the power that can be extracted in this fashion is proportional to the velocity cubed,

$$P \propto \frac{1}{2} c_D \rho A V^3 . \quad (0.3)$$

Improvements to the coefficient c_D are fairly limited; the density of water is given. Since the velocity is limited to less than the wave induced flow velocity, which is on the order of 1m/s, the only other means to increase power output is an increase in the area A of the element. This leads to large, and (in the case of storm surges) vulnerable structures with limited power output. One approach to improve this situation can be seen in the second class of wave power devices shown in Figure 1, designs 8-11. Here, a hydrodynamic transmission of one sort or the other is employed to increase the velocity at the mechanical power generating device, typically an air or water driven turbine. However, while making the turbine much smaller in this case, a large secondary structure like a duct or channel is needed to achieve this transmission. Thus, all that has been achieved is a shift of the cost and exposure to storm damage to the secondary structure.

It is noteworthy that none of the devices in Figure 1 interact with the wave flow directly exploiting *lift* as, for example, a state of the art windmill does. The entire wind power industry has transitioned in the last decades to lift based devices with a high tip speed ratio, which is the ratio between the velocity at the tip of a windmill blade and the wind velocity. To first order, the power that can be extracted by a same size windmill blade is thus increased by the tip speed velocity cubed. For windmills, this has vastly improved efficiencies and reduced cost. In addition, it leads to higher Reynolds number flow at the blade, which from a fluid dynamic perspective is less prone to detrimental flow separation.

These considerations led to the conception of the device proposed in this document. The proposed research investigates the Cycloidal Propeller as an improved wave power extraction device that operates at significantly higher blade speeds than the wave induced velocity. Due to the very small wave induced velocities, one would expect this transition to lead to even more dramatic improvements in energy extraction than have been realized in wind mills.

Cycloidal Propellers

Cycloidal propellers have a long history of use for propulsion of highly maneuverable marine vessels such as tugboats and ferries. Patented in 1931 by Darrieus [11], they are also known as Darrieus turbines or, after the German inventors of these devices, Voith-Schneider propellers. Their main advantage is the ability to produce thrust in any direction normal to the propeller shaft. A typical cycloidal propeller has its main shaft oriented vertically, and consists of a set of two-dimensional foils attached to a rotating disk as shown in Figure 2b. These blades change their angle of attack by rotating relative to the disk for each revolution, which is typically accomplished by a mechanical pitch control mechanism (not shown). In marine applications, cycloidal propellers have been almost exclusively used for propulsion to date, even though their use for energy extraction of marine tidal currents has been proposed [12]. In air, on the contrary, cycloidal propellers are used almost exclusively as windmills and are mostly referred to as vertical axis wind turbines (VAWT), named for the typical orientation of the main shaft. While their efficiency is similar to that of the more common horizontal axis wind turbines (HAWTs), both structural and economical considerations favor the horizontal axis turbines for large scale power production. However, VAWTs perform better in gusty wind conditions and are therefore currently being developed for use in distributed power generation in grid connected applications in urban environments [13]. This

improved performance is attributed to the fact that VAWTs do not need to be aligned to the wind in changing wind conditions, but can extract energy from any flow perpendicular to their shaft.

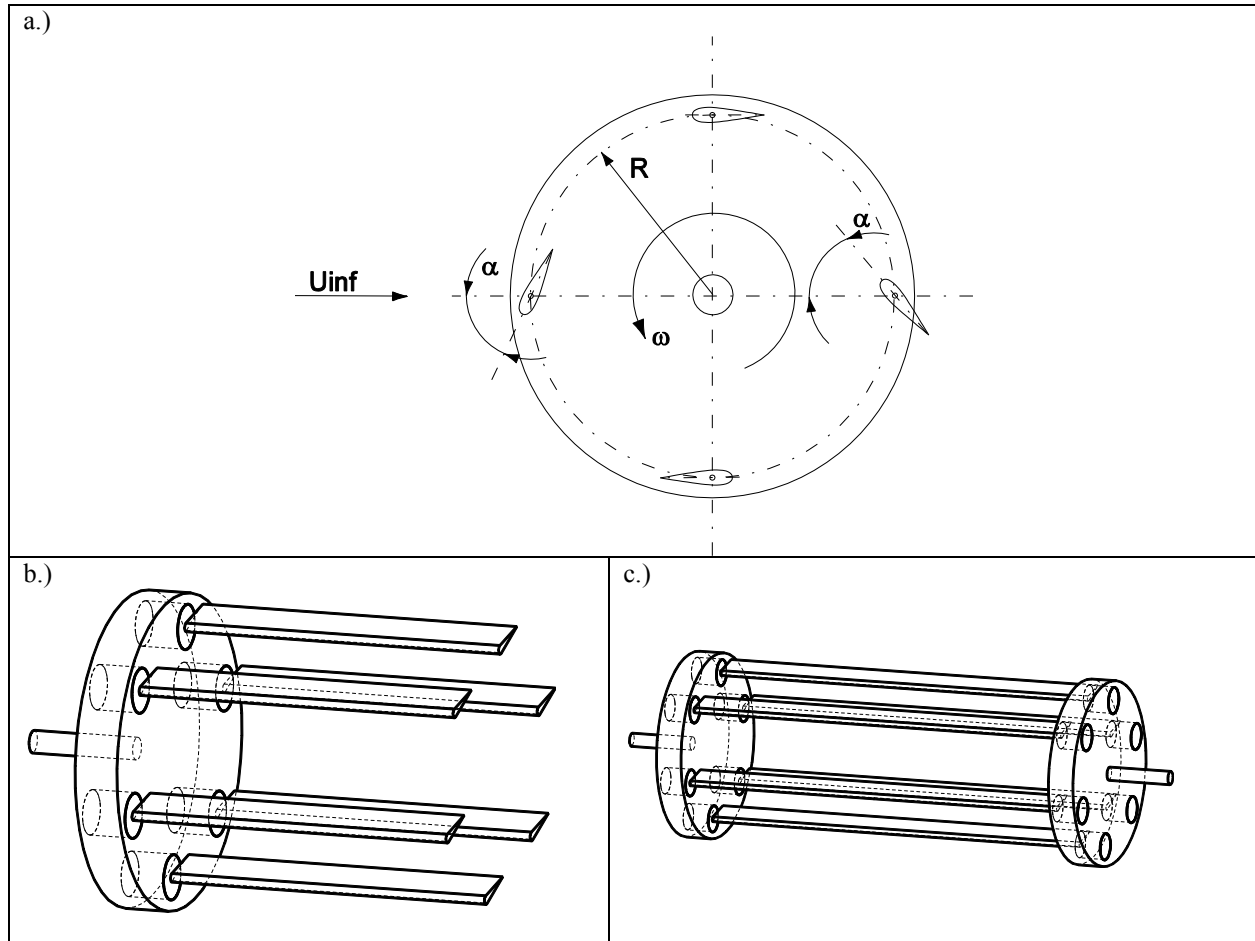


Figure 2: a.) Cyclical Propeller with four blades, b.) 6 blade single end disk propeller, c.) 6 blade double end disk propeller.

These previous studies indicate the suitability of a cycloidal propeller for energy extraction from unsteady flow fields, which is the exact situation in which a wave power converter operates. In fact, Darrieus himself suggested the use of cycloidal propellers for wave power extraction. However, there are additional obstacles that need to be overcome before a cycloidal propeller can be used for wave power extraction.

Adaptation of a cycloidal propeller to wave power extraction

Two main improvements are needed in order to use a cycloidal propeller for wave power extraction. The first issue is the interaction of the cycloidal propeller with the wave induced flow. While the blades of cycloidal propellers used for propulsion can be pitched in a predetermined fashion depending on the desired direction of thrust, a cycloidal propeller used for wave power extraction will need to pitch its blades in response to the instantaneous direction and magnitude of the wave induced flow. Thus, both flow sensors and a controller are needed in addition to the ability to change the pitch of each individual

blade of the propeller. This leads to a device that requires *feedback flow control* for successful operation, an area of expertise that has been developed in recent years under AFOSR funding by the PI and senior personnel involved in this proposal.

The second issue is that due to the low flow velocities in waves, it is advantageous to employ dynamic lift as is used by many animals for aquatic propulsion and avian flight. A preliminary study conducted by the PI [14],[15] further developed the well established Cycloidal Propeller for operation at very low Reynolds numbers. By implementing a sinusoidal pitching schedule in the rotational cycle of a Cycloidal Propeller, dynamic lift can be exploited at a Reynolds number of 10,000, where the flow over the airfoil otherwise would be fully stalled. The study conducted with AFOSR small grant funding [14] demonstrates the ability of a Cycloidal Propeller to perform propulsion or energy extraction in a steady flow efficiently at low Reynolds numbers. Without detailed optimization of pitch schedules, efficiencies of greater than 55% were demonstrated. This is an enabling technology for wave power extraction, where large amounts of energy are present in the form of very low velocity fluctuations (typically less than 1 m/s peak velocity). A patent application for this type of Cycloidal Propeller has been granted by the U.S. Patent and Trademark Office [16] [17].

Experimental Work

There are two distinct phases to the experimental work performed to date. In the first two years, a cycloidal turbine or propeller with a vertical shaft was constructed, and tested in the Air Force Academy water tunnel in steady flow. In the second year, these experiments were extended to unsteady, fluctuating flow fields using the same setup that are a good representation of a shallow water wave. The latter experiments required the use of a flow sensor along with a feedback controller for efficient energy conversion.

In the second phase of experimental work, a new wave tunnel facility complete with a flap type wave maker and beach was constructed at the Aeronautics Laboratory, which at the writing of this document is functional and has been instrumented with wave gauges. This tunnel is capable of creating both intermediate and deep water waves and can thus be used to show wave energy conversion using the CycWEC for waves that cannot be simulated by the water tunnel experiment. The CycWEC has two blades and a horizontal, submerged main shaft that is parallel to the incoming wave crests. It has been designed and constructed, and is expected to become operational shortly. This setup will be used in the third year of this program to validate numerical simulation results for deep and intermediate ocean wave cancellation. The following sections detail the results in both experimental areas, followed by the numerical simulation result section.

Water Tunnel Cycloidal Propeller Experiments

The year one effort on the experimental side of the research program was focused on development and testing of a cycloidal turbine in steady flow in the US Air Force Academy water tunnel. This turbine serves several purposes. During the first year, initial testing in a steady flow environment allowed for comparison with existing data from open literature for validation of the setup. Subsequently, software was implemented to design and test variable blade pitch schedules, for which little experimental data is available. The goal was to develop pitch algorithms that efficiently extract power for a large range of Tip

Speed Ratios (TSR = ratio of rotational blade velocity to free stream velocity). The TSR will typically vary in a wave induced velocity field, therefore this is a crucial development step for deployment of a Cycloidal turbine as a wave energy converter. We present successful results from both of these investigations in this section.

The final test of these pitch algorithms will incorporate a time varying (unsteady) flow field created by adjusting the tunnel velocity to simulate shallow water wave particle path velocities. A feedback control blade pitch algorithm will correspondingly adjust the blade pitch angles in real time using the measured varying flow velocities to achieve maximum power extraction. This research will start in the fall 2010 semester.

The capabilities of the current setup far exceed the state of the art for both Vertical Axis Wind Turbines (VAWTs) as well as cycloidal propellers like the Voith Schneider Propeller sold by Voith Hydro. While all commercial VAWTS feature a fixed blade angle, the Voith Schneider Propeller features a mechanical linkage system which does not allow for direct control of the angle of each blade. However, direct blade control is an essential capability for wave energy extraction due to the unsteady flow field.

Design goals and objective

In order to be successful at extracting energy from fluctuating velocity fields, the first design requirement is to have the capability of adjusting each blade's pitch angle with effective, real time feedback control software. This requirement led to the use of individual direct drive servo motors for each blade. The direct drive setup enables measurement of the shaft torque without any additional hardware by monitoring the current in the motor windings, which is directly proportional to torque. In addition, for feedback flow control of the flow around individual blades, at least an integral flow state measurement needs to be available. The simplest and most important quantities that can be measured easily are the blade normal and tangential forces. In order to measure these, a custom developed force balance is being employed. While all of these requirements are relatively straightforward in and by themselves, they become difficult to implement in combination and more importantly, in the context of a rotating turbine.

Mechanical setup

The mechanical setup was kept as simple as possible by orienting the main shaft of the Cycloidal turbine vertically, which allows for placement of the turbine hub along with electronic components above the water level outside the tunnel. Also, using this approach reduces the amount of flow blockage caused by the relatively large size of the blade mount and motors. An aluminum suspension frame houses two main shaft bearings, a slip ring assembly and the main shaft servo motor controller and main shaft motor, see Figure 3 for a CAD drawing and Figure 4 for a picture. The model is modular in nature, allowing for different numbers of propeller blades, which can be attached to the propeller hub at different radii of 16, 14 and 12 cm. In a similar fashion, the blades are exchangeable. For the results presented here, a blade chord of 50mm with a symmetric NACA 0015 hydrofoil was employed. The archetypical model protrudes into the tunnel by a span of 450mm. Each foil is attached to the shaft of the blade motor directly at the quarter chord of the foil from the leading edge. This setup allows for instantaneous adjustment of the pitch angle of each blade. Furthermore, the mounting of each blade to

the propeller frame is implemented with two sets of flexures that are instrumented with strain gauges, allowing for measurement of the tangential and radial force components.

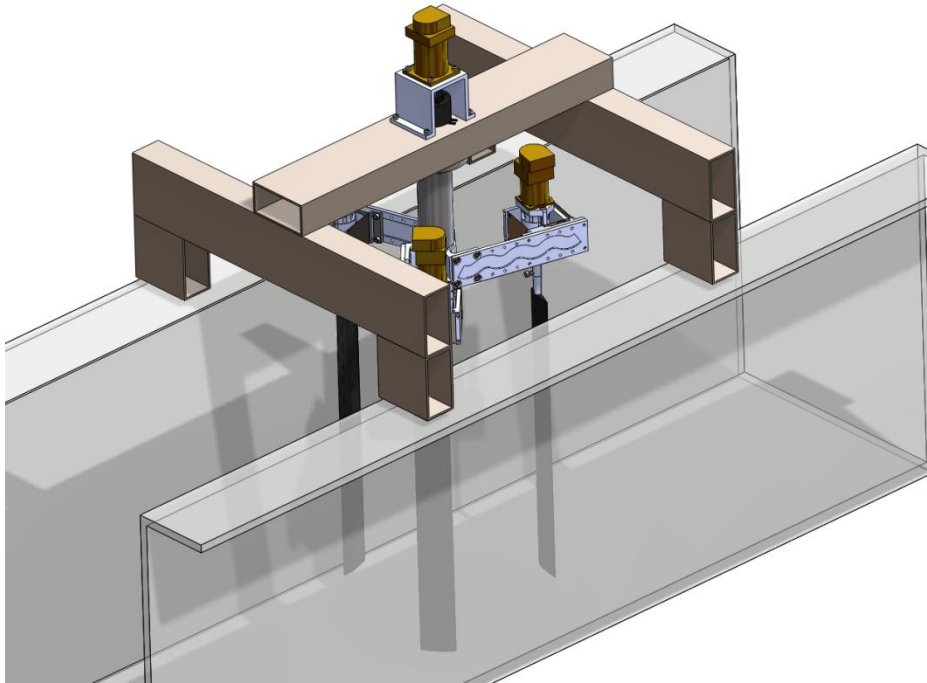


Figure 3 CAD Design of cycloidal turbine water tunnel model. Black, turbine blades. Brass, servo motors. Tranlucent, water tunnel test section

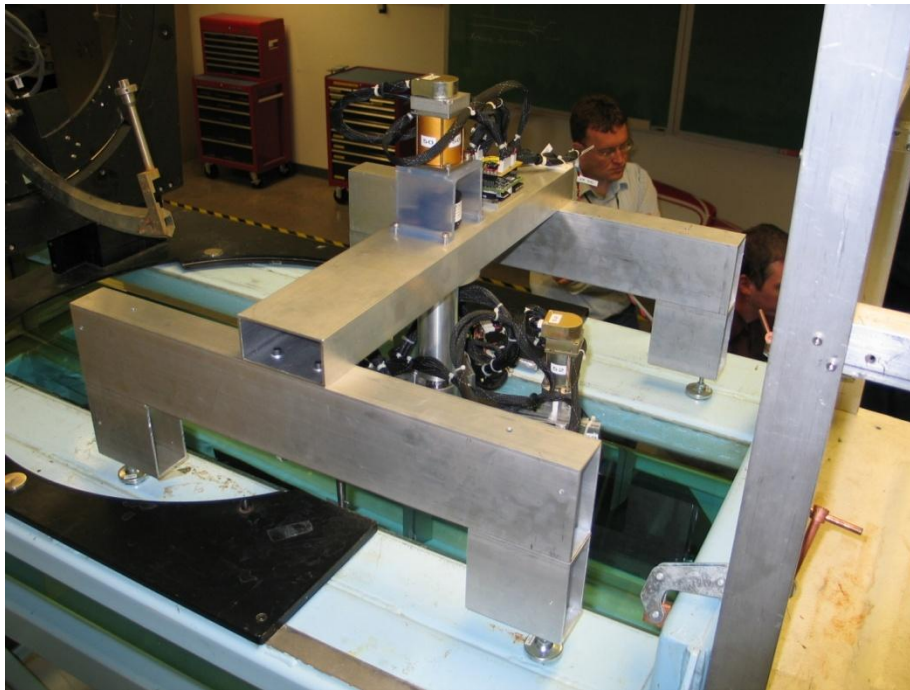


Figure 4 Picture of cycloidal propeller in water tunnel

Electrical and software design

One of the main challenges of the electrical setup is that each measurement signal, control signal and power supply line must pass through a slip ring assembly, which becomes an electromagnetic interference problem when both high current power (for the motors) and low voltage measurements (force balance strain gauge signals) are involved. To overcome this problem, it was decided to employ the latest technology in distributed process control allowing for the integration of the servo controllers as well as data acquisition modules on the rotating turbine, thus minimizing electromagnetic interference by using short signal lines, and also reducing the connections through the slip ring assembly to two power and one network connections. As shown in Figure 5, the entire electrical setup relies on a Controller Area Network (CAN) bus system to exchange data between a main control computer running a real time operating system, and each of the four motor controllers operating the main shaft and blades. Also, the strain gauge measurements from the force balances are transmitted over the same bus system.

The CAN bus operates at a data rate of 250kbps, which allows for update rates of all network transmitted variables at a cycle time of 8ms, which is a more than sufficient sample rate given that the rotational frequency of the cycloidal turbine does not exceed a few Hertz. The real time operating system programmed in LabVIEW ensures deterministic loop update rates during measurement runs. The software currently implements pitch cycle control without feedback, but does allow feedback controller implementation in the upcoming measurements with variable tunnel speed. The different pitch cycles are outlined in the next section.

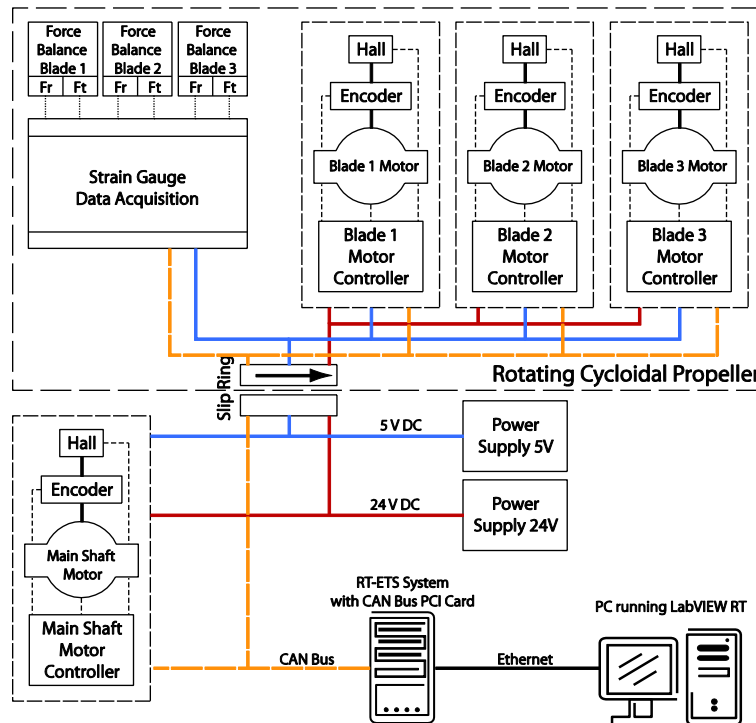


Figure 5 Electrical Setup

Experimental Results

The schematic in Figure 6 shows a top view of the cycloidal turbine installed in the water tunnel, along with the coordinate system in which the data in this section will be presented. A rotational cycle of the main shaft starts at the top of the circular path where the blade travels in the upstream direction, and the main shaft rotates in the counter clockwise direction. Similarly, the blade pitch angles α are also measured positive in the counter clockwise direction, relative to a body fixed reference system for each propeller. Thus, a blade at a fixed pitch angle of 0 degrees will always point in the tangential direction.

The main operational parameter of the propeller is the tip speed ratio or TSR:

$$TSR = \frac{\omega R}{U_\infty} \quad (0.4)$$

And the main non-dimensional result that determines the efficiency of the Cycloidal turbine is the power coefficient c_p :

$$c_p = \frac{\omega T}{\frac{1}{2}\rho U_\infty^3}. \quad (0.5)$$

In the above equations, U_∞ is the free stream velocity, ω the rotational frequency of the propeller in radians, R the propeller radius, T is the main shaft torque, and ρ the fluid density.

The results presented here employ two different pitch schemes; first, a fixed angle pitch scheme where the blades do not rotate with respect to the turbine was tested to establish baseline measurements for comparison to literature. Then, a sinusoidal angle of attack pitch scheme was tested where the pitch angle of the blades α_b is varied according to the equation

$$\alpha_b = \alpha_F - \hat{a} \sin \alpha_s \quad (0.6)$$

$$\alpha_F = \tan^{-1} \left(\frac{U_\infty \sin \alpha_s}{\omega R - U_\infty \cos \alpha_s} \right), \quad (0.7)$$

Where α_s is the main shaft angle and \hat{a} the peak angle of attack (AOA). α_F is the feather angle of the blade, at which the chord of the foil is parallel to the velocity direction relative to the blade. It should be noted that the feather angle calculation is strictly speaking only accurate for the upstream portion of blade travel, since on the downstream portion the incoming velocity will be less than U_∞ due to the interaction of the blade with the freestream velocity. Figure 7 shows the blade pitch angle as a function of main shaft angle for different tip speed ratios. It can be seen that for tip speed ratios below one, the blade is rotated by one revolution for each main shaft revolution. At a tip speed ratio of one, there is a discontinuity in the motion, which becomes less severe for larger tip speed ratios.

While the model allows for different radii to be used, the initial runs showed that the largest radius was yielding the best measurement results due to the reduced effect of artificial camber of the blades as well as reduced surface waves. Artificial camber is caused by the blade travelling on a circular path, causing a different flow angle at the leading and trailing edge of the foil. Thus, all results presented here are for a turbine radius of $R=160\text{mm}$. In a similar fashion, a water tunnel velocity of 150 mm/s was determined to be the optimal velocity to minimize surface wave and blade bending effects for a large range of tip speed ratios. In the initial investigation, tip speed ratios between 1.5 and 5.5 were considered, and lower tip speed ratios yielded poor power coefficients while larger tip speed ratios caused excessive blade bending. Also, at larger tip speed ratios surface waves became a significant factor.

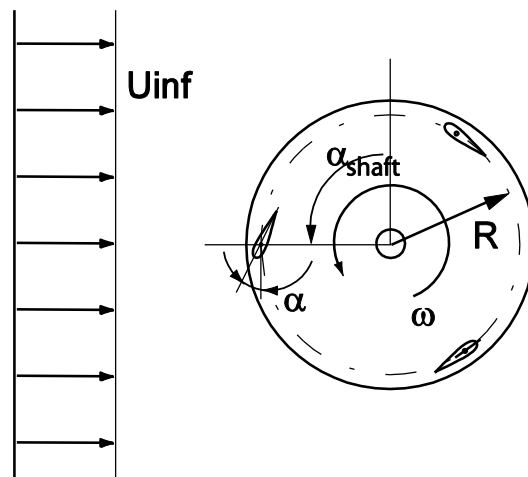


Figure 6 Coordinate system and variables, view from the top of the water tunnel.

The main shaft torque was derived from the main shaft current measurements from the servo amplifier, and converted from current to torque using the published torque constant from the manufacturer's data sheet. Since the goal was to measure the hydrodynamic forces, a dry run with the apparatus in air was performed and the torque necessary to spin the turbine in air was subtracted from the measured quantities in water. This should yield an accurate estimate of the hydrodynamically produced torque. In addition, a blockage correction was applied to the measured power coefficients based on a linear correction suggested by Werle [18].

The measurement runs presented here were conducted operating the main shaft in constant velocity mode. A linear ramp in velocity was prescribed following a settling period during which the exact rotational velocity was allowed to stabilize. Then, data was acquired for 20 to 40 rotational cycles depending on tip speed ratio, using a stable mean value as the criterion to establish the necessary number of rotations. The data was then averaged over these cycles, or phase averaged to determine the torque as a function of main shaft angle. For phase averaging, the data was collected in bins of 10 degrees based on the main shaft angle and averaged.

Runs with several fixed pitch angles are shown in Figure 8. The first observation is that the power coefficient is very sensitive to small changes in pitch angle; at a tip speed ratio of 4, plus or minus one degree changes the power coefficient from -0.4, to zero, to 0.2. The maximum power coefficient is on the order of 0.2 and thus relatively small, indicating the potential for improvement using a better pitch control scheme. Also, the tip speed ratio range for which a positive c_p can be achieved is small, ~ 2.5 -5.5 in the best case. The fact that a negative pitch angle yields the best result can be explained by the artificial camber effect caused by the otherwise symmetric airfoil traveling on a curved path, which will yield a lift force at zero angle of attack that is clearly detrimental to energy conversion.

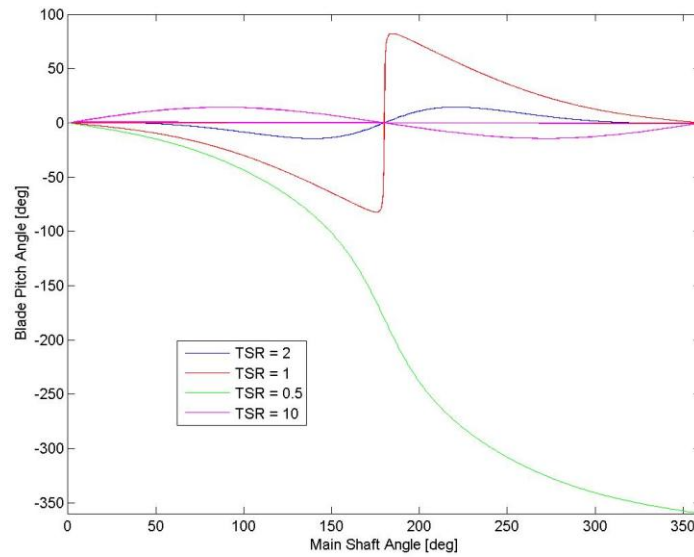


Figure 7 Blade Pitch angles for different TSRs. Sinusoidal angle of attack pitch schedule with a peak angle of 20 deg.

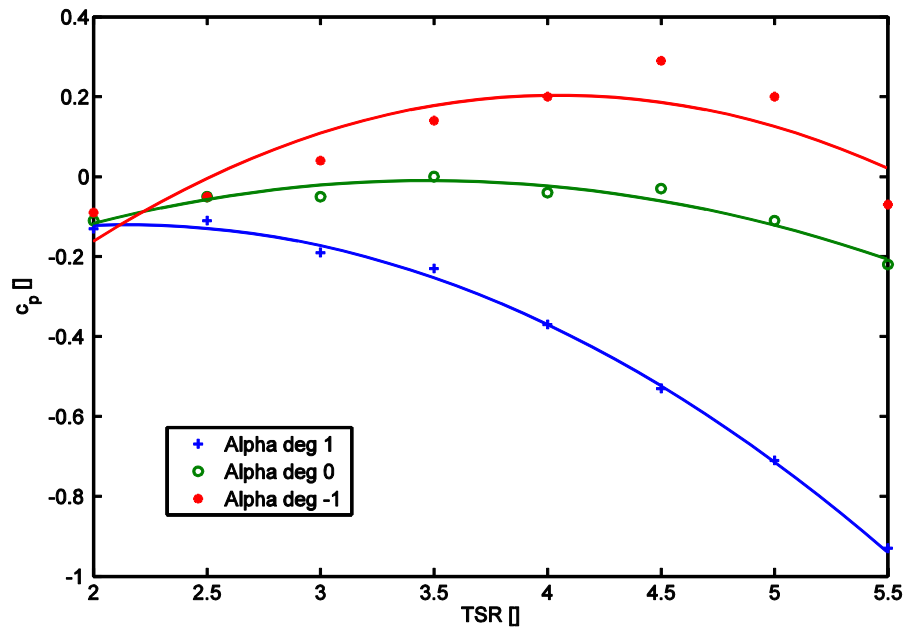


Figure 8 Power Coefficient for fixed blade angles at tip speed ratios between 2 and 5.5. $U_\infty = 150$ mm/s, $R=160$ mm, 3 Blades. The symbols represent measured data, the lines are a second order polynomial fit.

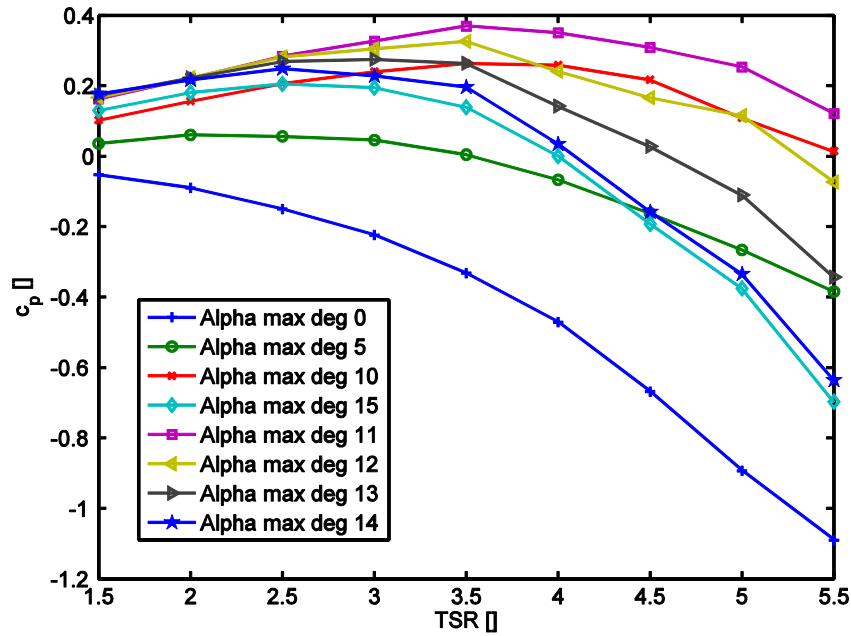


Figure 9 Power coefficient vs. tip speed for sinusoidal angle of attack pitch schedule with various maximum pitch angles. $U_\infty=150$ mm/s, 2 Blades, $R=150$ mm

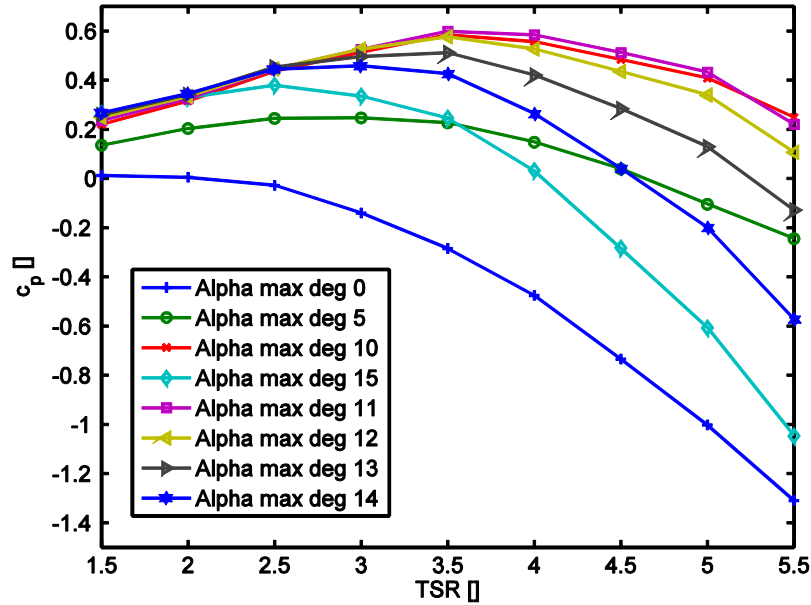


Figure 10 Power coefficient vs. tip speed for sinusoidal angle of attack pitch schedule with various maximum angles of attack. $U_\infty=15\text{cm/s}$, 3 Blades, $R=15\text{cm}$

The data shown in Figure 9 demonstrates the sinusoidal pitch scheme described in the beginning of this chapter. For an optimal peak angle of attack (AOA) of 11 degrees, and the most efficient TSR of 3.5, a C_p of now 0.35 can be achieved using fewer blades than in the fixed pitch runs shown in Figure 8. Stall is most likely limiting the resulting performance at high angle of attack, while at lower peak angles of attack, insufficient lift and consequently torque is produced to achieve an optimal power coefficient. A sharp drop in power coefficient can be observed for 12 deg peak AOA for tip speed ratios beyond the best TSR of 3.5, the reason for this is still under investigation.

Figure 10 presents the same pitch scheme and operational parameters as shown in Figure 9, however for three blades. The optimal tip speed ratio and angle of attack are identical to those seen in Figure 9, however, the maximal power coefficient has increased to close to the optimal theoretical limit of 0.59, compared to 0.35 for two blades. This indicates that at the moderate foil chord Reynolds numbers present in the current investigation, an increase in blade number still does improve the overall power coefficient. More insight into the fluid dynamic physics of the Cycloidal turbine can be gained by investigating the main shaft torque as a function of main shaft rotational angle. This data is presented in Figure 11 for the same operational parameters as in Figure 10, i.e. 3 Blades with a sinusoidal angle of attack pitch schedule. All data presented is for a tip speed ratio of 4. The torque sign convention follows that of the current sign convention of the motor controller, where a negative current/torque denotes energy transfer out of the motor, while a positive current or torque indicates energy transfer to the motor. For a maximum angle of attack of 15 degrees, large fluctuations in torque are indicative of potential blade stall, while the torque curve is mostly flat for the other peak angles of attack. The torque observed for zero degrees pitch angle denotes the effects of skin friction only, since the blade is pitched parallel to the incoming flow. Large changes in torque can be observed for small changes in maximum

angle of attack around the optimal angle of attack of 11 degrees. We plan to further investigate the flow physics at the blade using the two component force balance setup in the near future.

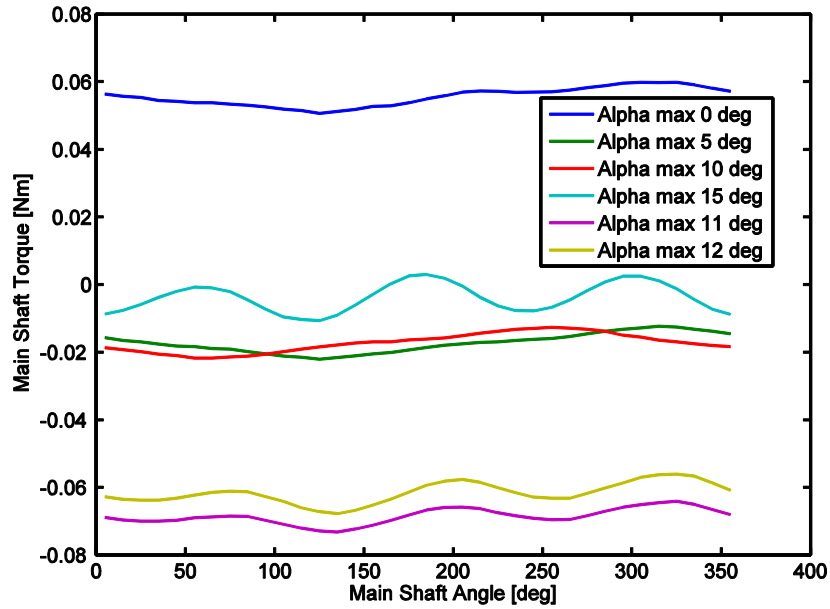


Figure 11 Main shaft torque vs. shaft angle, negative torque represents energy extraction from flow. Sinusoidal pitch schedule with different peak angles of attack. $U_{\infty} = 15$ cm/s, 3 Blades, $R=16$ cm, $TSR = 4$.

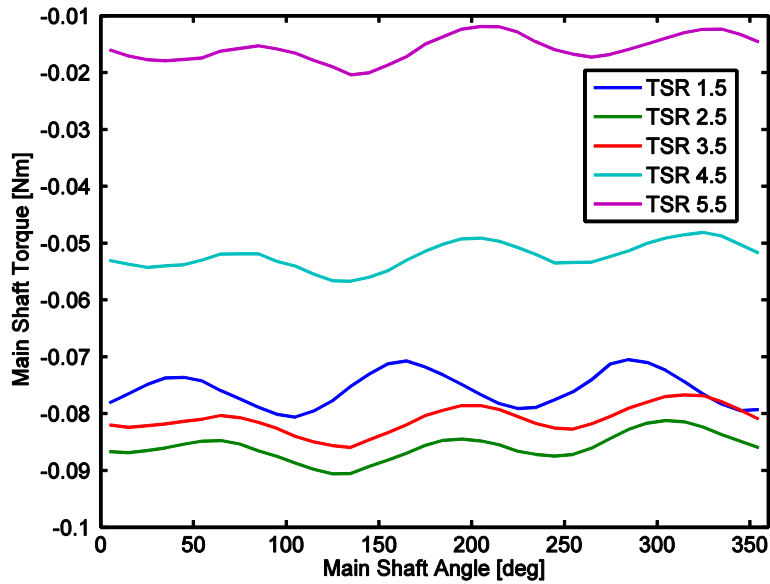


Figure 12 Main shaft torque vs. shaft angle, negative torque represents energy extraction from flow. Sinusoidal pitch schedule with different tip speed ratios at the optimal peak angle of attack. $U_{\infty} = 15$ cm/s, 3 Blades, $R=16$ cm, maximum AOA=11 deg.

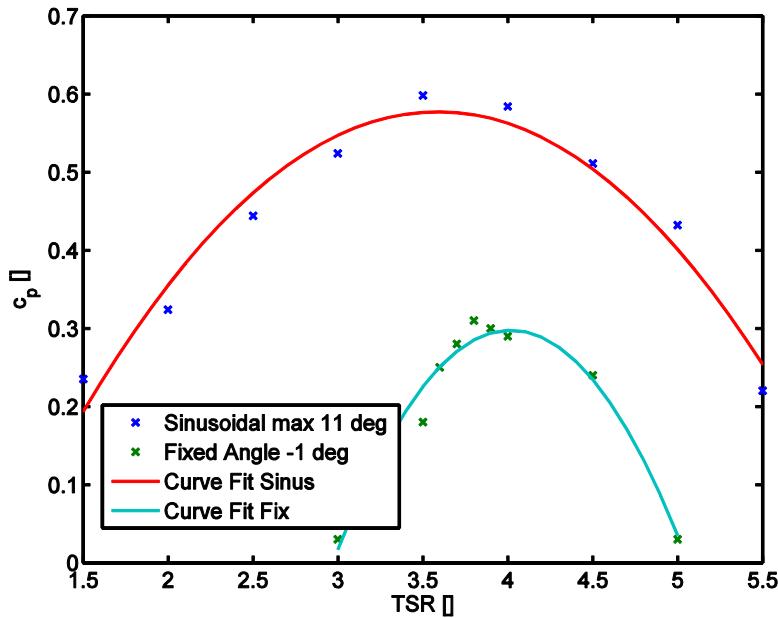


Figure 13 Comparison of best parameter choices for fixed blade angle and sinusoidal angle of attack pitch schedules. 3 Blades, $U_{\infty}=15\text{cm/s}$, $R=16\text{cm}$.

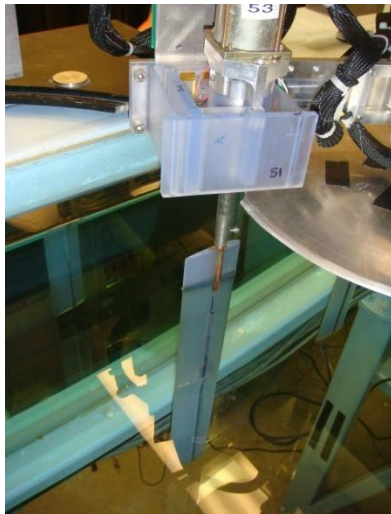
Figure 12 shows the effect of tip speed ratio on the main shaft torque. The maximum torque shifts to higher angles for higher TSRs, an effect that is still under investigation. Again, at the optimal tip speed ratio, only small torque fluctuations can be observed, with larger fluctuations at non-optimal tip speed ratios.

The main achievement of this measurement campaign is summarized in the data presented in Figure 13. While the fixed pitch schedule only delivers a usable tip speed ratio range of about three to five, the sinusoidal pitch schedule delivers power for all tip speed ratios investigated. Furthermore, the maximum power coefficient has more than doubled using sinusoidal pitching. We consider these results an important milestone in adapting the cycloidal turbine to use as a cycloidal wave energy converter.

In upcoming measurement campaigns, we plan to further investigate flow physics at the blade using both flow visualization and force balance measurements. In addition, we will operate the water tunnel to produce a fluctuating flow field similar to a shallow water wave. Using instantaneous flow measurements along with a feedback controller, we plan to optimize power extraction from this fluctuating flow in the second year of this program. Also, Laser Doppler Velocimetry will be employed to measure velocity profiles in the center of the propeller, with the goal to optimize the downstream pitch schedule by providing accurate estimates of the velocity encountered by the blades in the downstream portion of the cycle. This should allow for further improvements of power conversion efficiency.

Shallow Water Wave Energy conversion

The experiments in year two required additional experimental apparatus as described in the following:



Source:
Meid

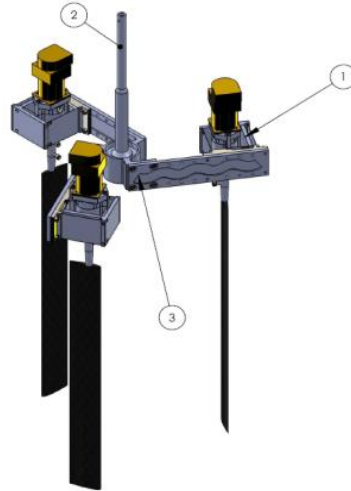


Figure 14: Force balance on blade assembly.

Figure 14 shows the force balance used by Skogsberg and Roland [3]. Each propeller blade assembly is composed of a mounting bracket (1), Hydrofoil Shaft Bracket (2), Blade Servo (3), NACA 0015 Hydrofoil (4), Hydrofoil Shaft Connection (5), and Motor Bracket (6). This set-up can be seen in schematics of Figure 14. Blade 3's Hydrofoil Shaft Bracket will be replaced with the force balance. As seen in the photo in Figure 14, the force balance, light blue, is simply the hydrofoil shaft bracket with 2 full bridge strain gauge assemblies placed on it. One of the assemblies measures F_t and the other F_r .

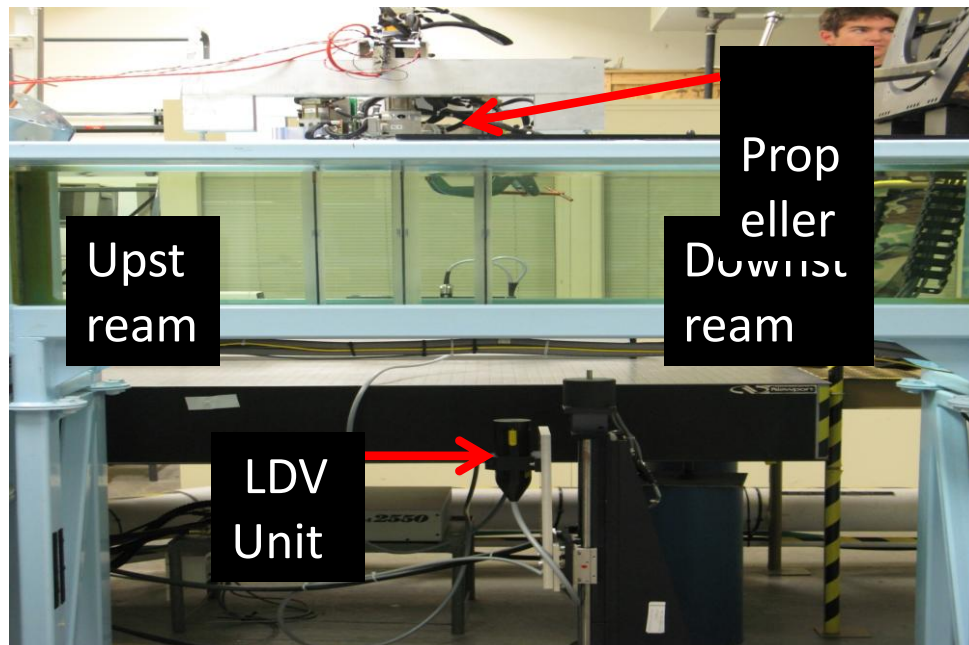


Figure 15: Experimental setup for LDV experiments.

Figure 15 shows the experimental setup used by Judd and White. It consists of the water tunnel the 3-bladed cycloidal propeller with variable pitch control at each blade and the LDV system placed under the water tunnel. The LDV is on a traverse system such that it can reach points upstream, midstream, and downstream of the propeller system.

Figure 16 and Figure 17 show the ADV used by Huxley and Hartman [5] as well as a flow diagram for their experiments. The ADV measures the speed of the water by emitting a high frequency acoustical signal, which is naturally reflected by the particles of a seeding material. Each of the four prongs shown in Figure 4 contains a microphone that receives the reflected frequencies. Those frequencies received by the prongs, are then sent to be reduced by the adjacent processing unit that determines the speed of a sample volume of water by use of the Doppler Effect Theory. This apparatus requires that the water tunnel be seeded with a substance of borosilicate glass beads in order to increase accuracy of readings.



Figure 16: Acoustic Doppler Velocimeter.

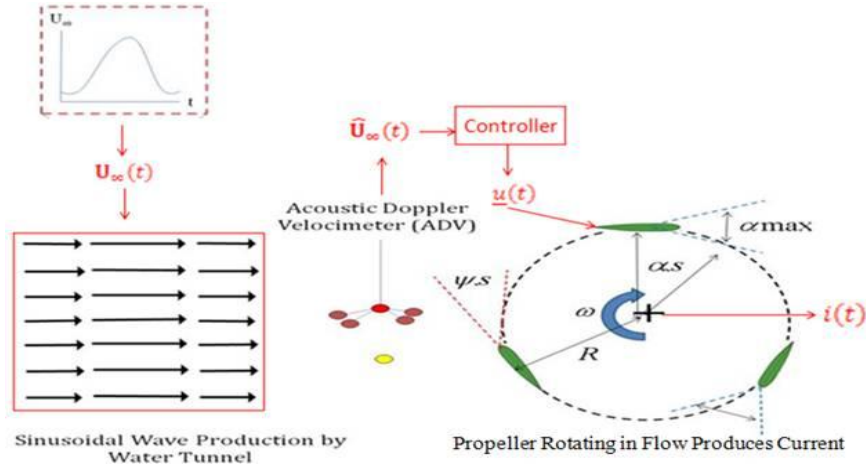


Figure 17: Flow diagram of feedback control using the ADV.

The year two experiments relied on these findings and the experimental results leading to the successful energy extraction from a simulated shallow water wave under feedback control are now presented.

The aim of the LDV wake measurement work of Judd and White [6] was to improve the blade pitch schedule. The LDV traverse system allows for velocity measurements to be made in upstream, midstream, and downstream segments of the water tunnel as depicted in Figure 15. Figure 18, for the case of 11° max pitch angle, shows typical velocity profile measurements. The blue line shows the constant upstream velocity. In contrast to the steady state upstream flow, the midstream flow was expected to be turbulent with a slowed wake profile as seen above. The left side of the wake speeds up and the right side slows down due to the direction the cycloidal propeller spins and tunnel blockage; this is the main cause of the lopsided velocity curve. This is theoretically reasonable due to the fact that the front side of the propeller extracts energy out of the water flow, thus slowing down the overall water velocity prior to the back side of the propeller. Finally, when comparing the midstream data with the downstream data it can be seen that some energy was extracted but nowhere near the amount the upstream blades were extracting. The highlighted area in Figure 19, for the case of 13° max pitch angle, shows the energy extracted from the flow is proportional to the area between the curves. Figure 19 shows similar findings as Figure 18, yet the comparison of the midstream and downstream data is where the story is told. When looking at the difference between the midstream and the downstream velocities there is really no area between the two curves. At a max AOA of 13° the midstream velocities are slightly lower but the downstream velocities are almost exactly the same, this is even more so in results for an AOA 15° . These findings point to the conclusion that the blades are not extracting energy during the downstream portion of the rotation.

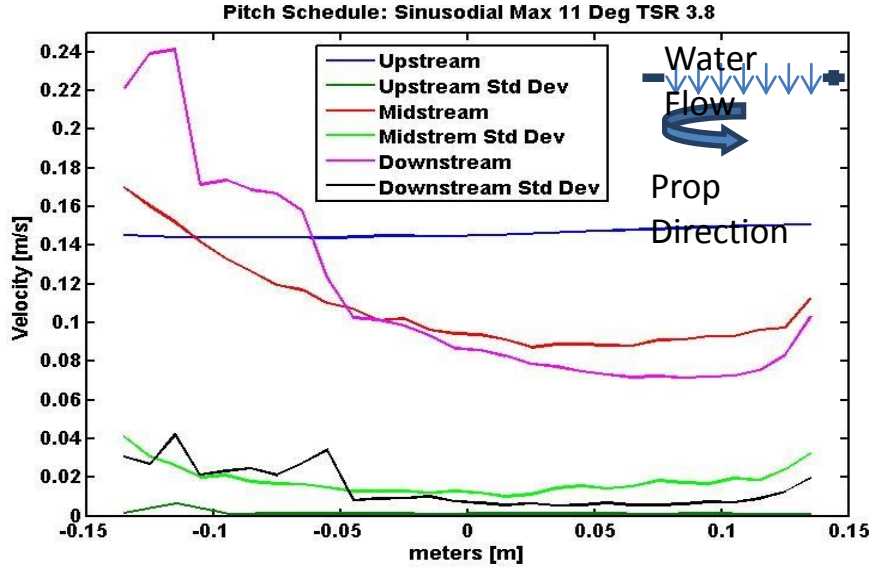


Figure 18: Velocity across the test section, sinusoidal 11° TSR 3.8- Up, Mid, Down Stream Data.

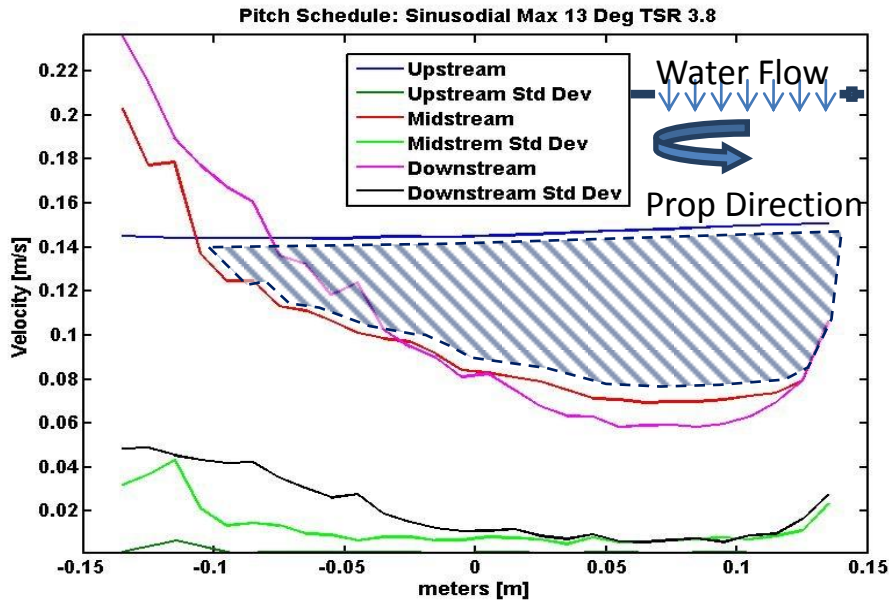


Figure 19: Velocity across the test section, with energy extracted for Sinusoidal 13° and 3.8 TSR.

After considering possible reasons for why the downstream blade was not extracting energy, a re-analysis of the angle of attack of the blades was performed. When the water tunnel velocity decreases in the midstream due to the disturbance of the upstream blade, the corresponding resultant vector of the flow velocity for the downstream blade becomes closer to the tangential direction. This effectively reduces the angle of attack of the downstream blade. Therefore it was determined that an asymmetrical sinusoidal pitch schedule should be implemented. Figure 20 and Figure 21 correspond to a sinusoidal and asymmetric sinusoid pitch schedule respectively. The asymmetric sinusoid of Figure 21

has a larger max pitch angle during the downstream portion of the cycle (dashed line represents angle of attack in the Figures).

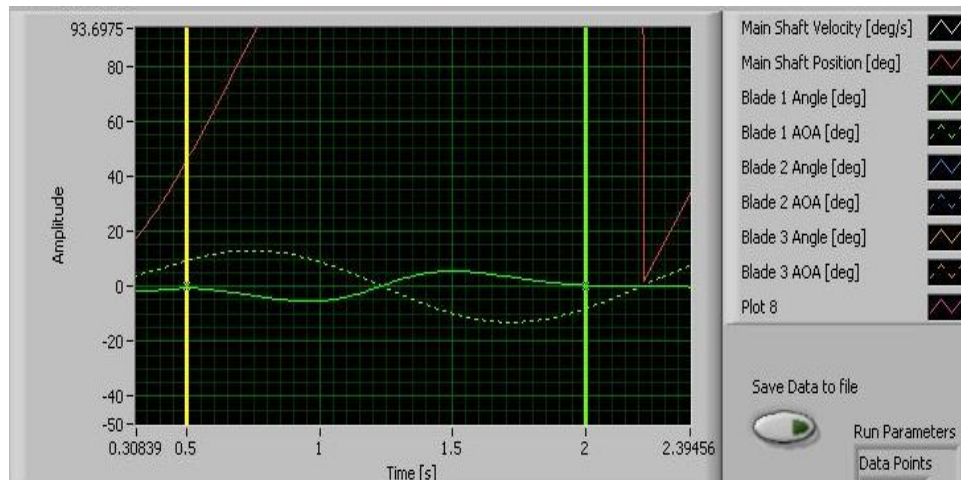


Figure 20: Labview Sinusoidal AOA vs Blade Angle.

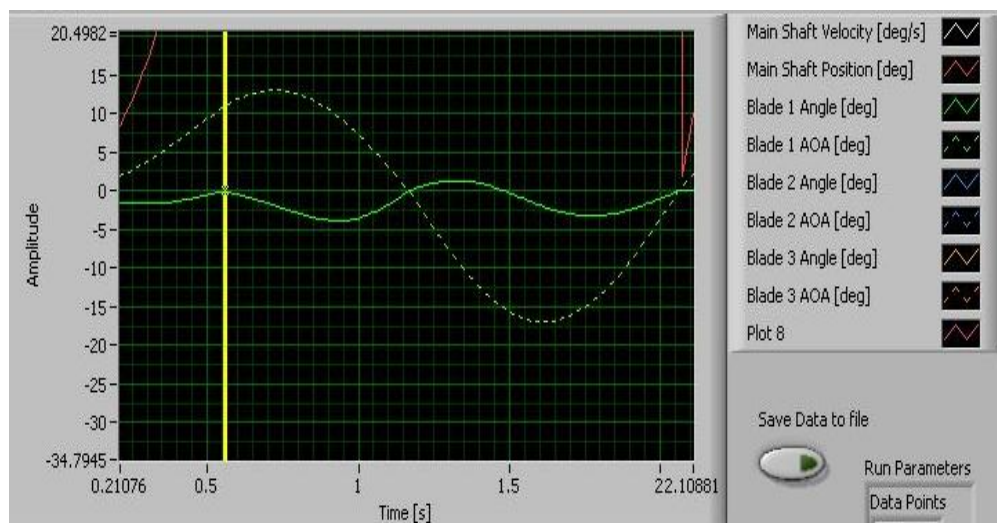


Figure 21: Asymmetric Sinusoid vs Blade Angle.

After performing experiments to find the optimal pitch schedule, the best pitch schedule was found to be an asymmetric sinusoid with a max AOA of 13° on the front side and a max AOA of -17° on the back side of the propeller's revolution. Figure 22 below shows the velocity profiles for the 3 segments of the water tunnel for this pitch schedule. Clearly the area between the midstream and downstream segments indicated energy extraction by the downstream blade resulting in this asymmetric sinusoid pitch schedule improving overall energy extraction. Figure 14 below shows an approximately 27% increase in average power coefficient versus using a symmetric sinusoidal pitch schedule.

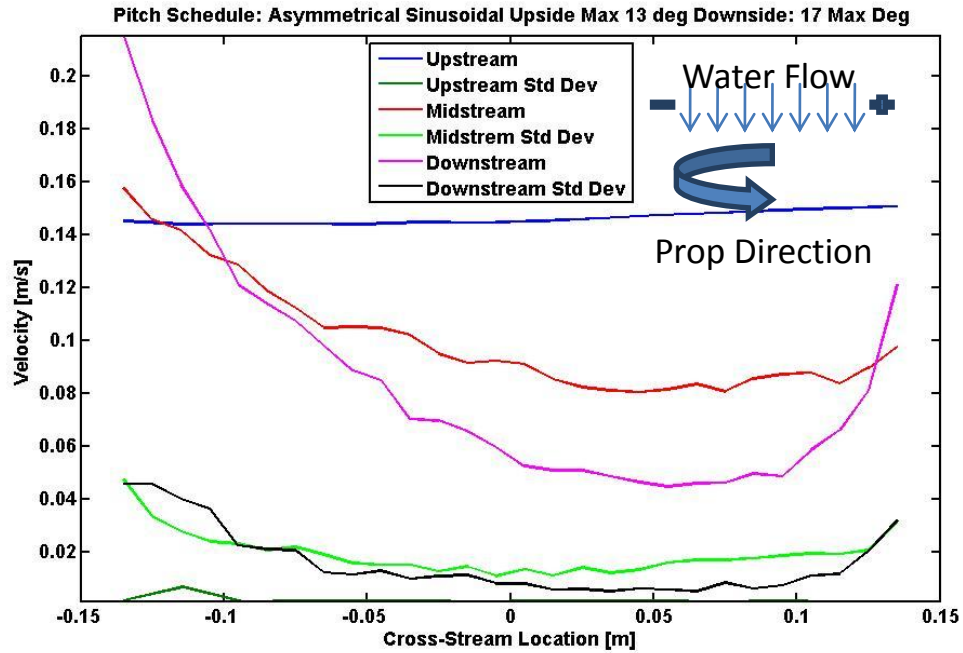


Figure 22: Asymmetric Sin Max 13°, Sin Max 17°

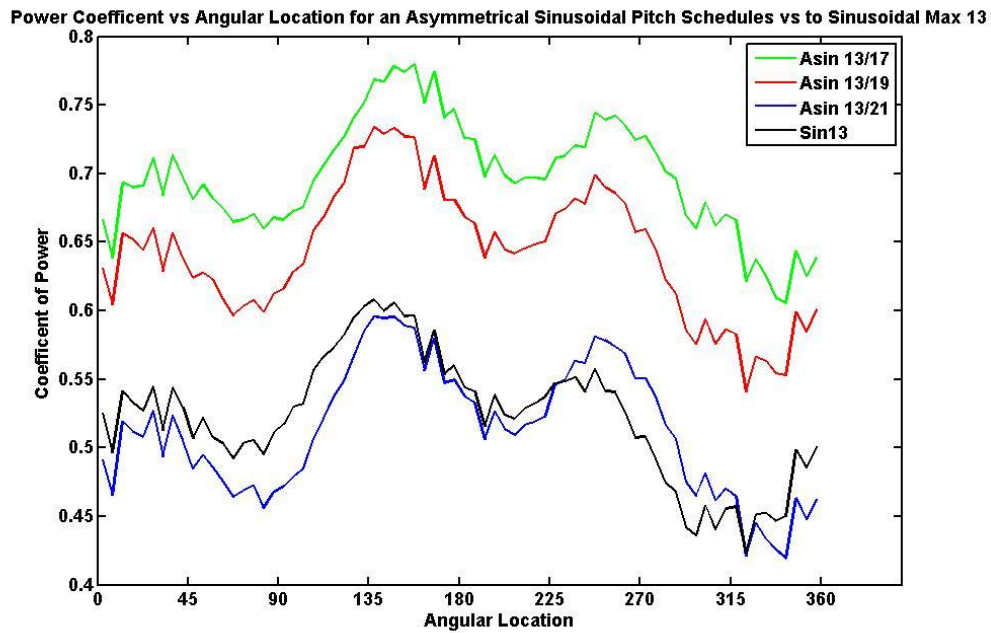


Figure 23: Power Coefficient of Asymmetric Test Trials vs. Sinusoid pitch schedule.

The aim of the work by Huxley and Hartman [5] was to initiate research employing the cycloidal propeller in unsteady flow using feedback. In this regard they successfully determined the time

response of the water tunnel to changing input freestream speed and also validated the Acoustic Doppler Velocimeter.

The tunnel was tested over a broad range of input frequencies and magnitudes to determine the response of the tunnel to a given input. Specifically, the tunnel was run for 39 different forcing inputs. To process the large sweep of inputs, each measured tunnel response measured by the LDV was plotted against the input forcing function. A Fast Fourier Transform (FFT) was used to find the magnitude of the frequency associated with each tunnel response. This amplitude was then compared to the input amplitude, and the gain was calculated and plotted for all the frequencies in a Bode Magnitude Plot. The FFT was used in order to see if the spread of frequencies associated with each run was closely related or if they were very far off from each other. This is important to determine if there are any other random sources of error in velocity measurements.

Table 3 shows the tested input parameters that the tunnel was able to adequately produce. These being just the tested tunnel input parameters, the tunnel is expected to model any period greater than seven seconds.

Max Velocity	Period Range	Amplitude
0.16 m/s	7 to 15 Seconds	0.065 m/s

Table 3: Tested tunnel inputs.

After extensive testing it was determined to best model a wave with a minimum input of 0.16 m/s, with a minimum period of 7 seconds—minimum meaning any value larger than 7 seconds is appropriate – and amplitudes no higher than 7 Hz or 0.065m/s.

The ADV was validated after much experimentation with the positioning of the device and the level of flow field seeding with borosilicate glass beads. Further experimentation with the signal strength and the use of moving averaging software successfully reduced the noise in the ADV signal.

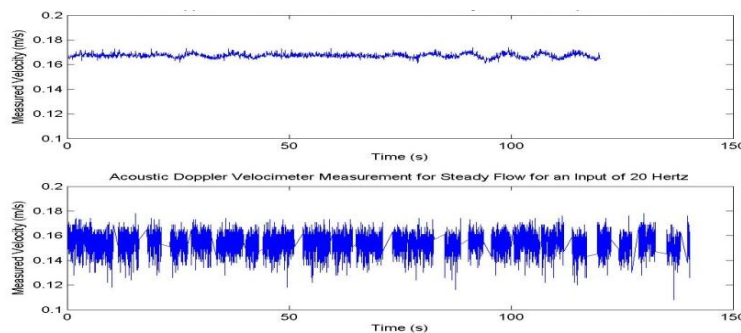


Figure 24: Noisy ADV signal (bottom) compared to. LDV signal (top).

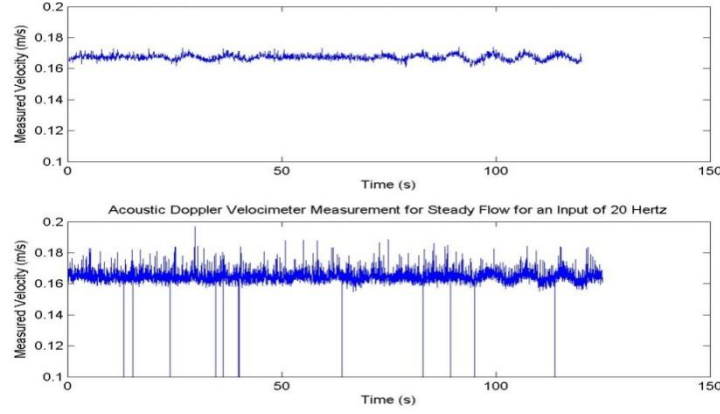


Figure 25: Improved ADV signal (bottom) compared to LDV signal (top).

Figure 24 and Figure 25 show the comparison of the ADV signal versus the LDV signal with and without the additional seeding of borosilicate glass beads to the flow field. The ADV validation was a major stepping stone for completion of this research. Without the ADV the feedback mechanism necessary for handling unsteady flows is not possible, as described in the design goals and objectives section.

The work of Boyd and Weakley [7] continued the efforts to extract energy by the cycloidal propeller from unsteady flows through feedback control. In previous work it had been determined that the optimal TSR was dependent on U_∞ , implying that the non-dimensional parameter of TSR does not alone capture the whole flow physics for this type of blade and fluid flow interaction. The question of how to adapt TSR for an unsteady flow needed to be addressed. With this in mind, their tests were designed to fulfill three individual objectives to accomplish the overall purpose of maximizing power extracted from ocean waves. The first objective is to find the relationship between average blade Reynolds Number and freestream velocity (U_∞) so as to maintain optimal power extraction. The second objective was to determine the relationship between the peak angle of attack during a blade revolution and power coefficient as defined by Equation 0.5. The final objective is to vary the feedback parameters of blade pitch angle (corresponding to peak angle of attack) and shaft rotational frequency ω (corresponding to average Re) to maximize power extraction from the unsteady flow.

Initial experiments were performed in steady state to find the relationship between average blade Reynolds number and freestream velocity for maximum power extracted.

The first objective required the freestream velocity to be fixed as the shaft frequency, ω is varied. In this way measurements were taken for a range of average Reynolds number defined as:

$$\overline{Re} = \frac{\omega R c}{\nu} \quad (0.8)$$

This procedure was repeated for five values of U_∞ and the results are shown in Figure 26. For the ideal case where TSR fully describes the propeller/flow interaction the five curves in the figure would collapse onto a single curve. Instead the figure shows separation between the curves and that there is an optimal average Reynolds number for each given freestream velocity where the power coefficient is maximized.

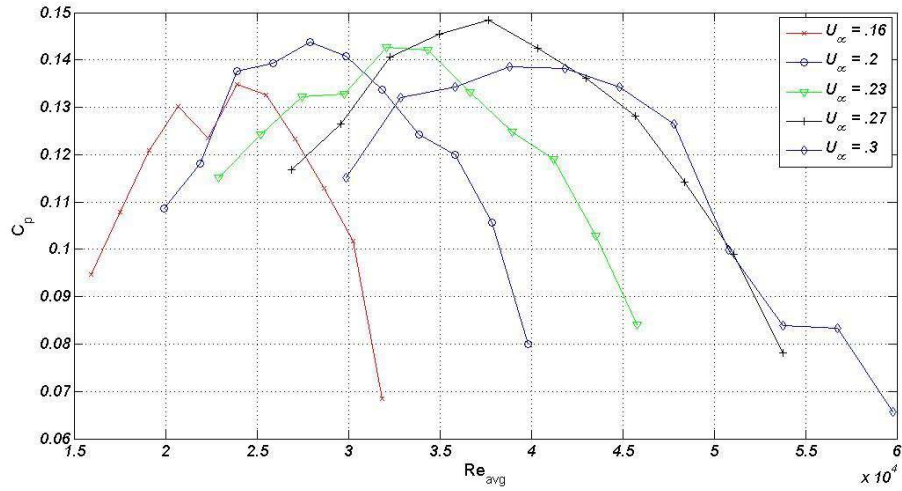


Figure 26: Power Coefficient vs. Average Reynolds Number.

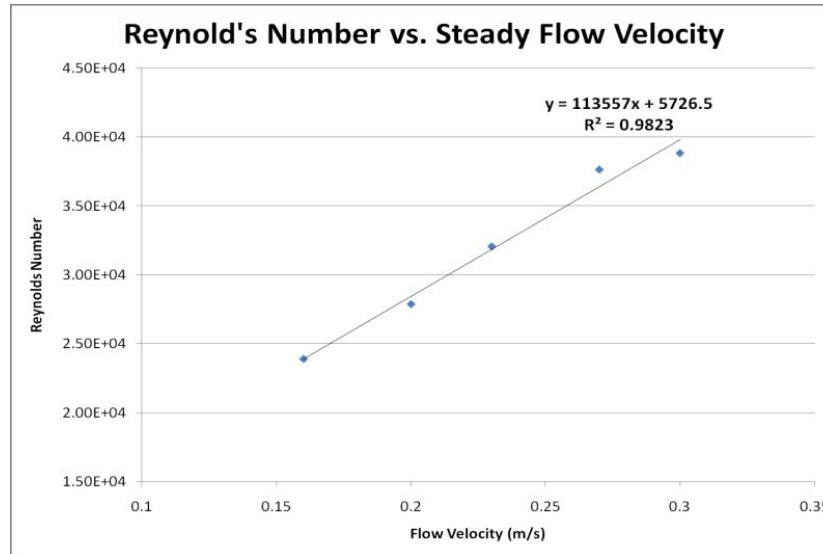


Figure 27: Average Reynolds Number vs. Flow Velocity for optimal c_p .

Based on the max power coefficient data from Figure 26, Figure 27 was produced and a linear relationship was determined between average Reynolds Number and freestream velocity for optimal c_p . This allows the average Reynolds number to be calculated for any tunnel velocity. The Reynolds number equation can then be rearranged to solve for ω . The relationship of ω versus U_∞ which yields optimum c_p is:

$$\omega = 2.268(U_\infty) + 0.1144 \quad (0.9)$$

This new equation for ω was coded into the controller and adjusts the rotational velocity of the blades to achieve the desired TSR values for the measured tunnel velocity. Analysis of the experimental data indicates that the optimal TSR range is between 2.6 and 3.0 for the operating range of this project.

Investigations into the effect of the peak angle of attack on the amount of power extracted at each velocity were also performed. The TSR was held constant at 3.0, which corresponds to the peak c_p from the first set of tests. Unlike the average Reynolds number, the peak angle of attack corresponding to the maximum c_p was unaffected by the change in the freestream velocity. Figure 19 demonstrates this.

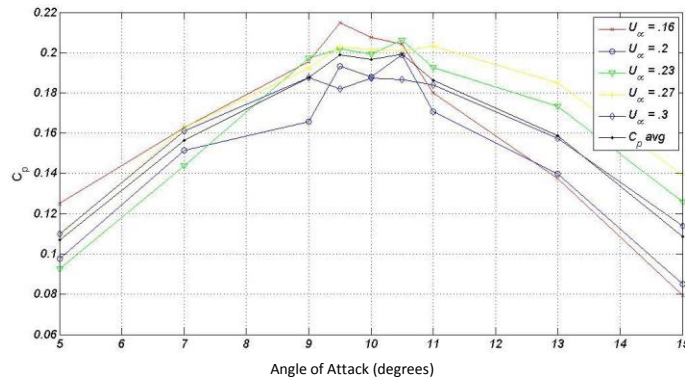


Figure 28: Power Coefficient vs. Peak Angle of Attack.

Therefore, the maximum angle of attack used for the unsteady flow tests was constant at 10.5° for all velocities. Given the low Reynolds number, this is most likely caused by flow separation occurring at higher angles of attack which detracts from the power coefficient due to an increase in drag.

Finally, tests were performed to investigate the operation of the cycloidal propeller in unsteady flow conditions. By varying the velocity of the tunnel flow over a period of time, a wave can be modeled as in Figure 29.

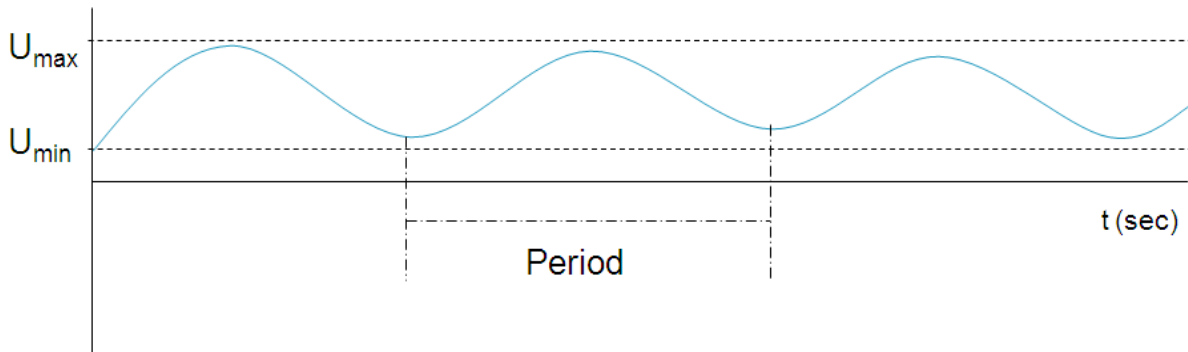


Figure 29: Tunnel Velocity Schedule.

For these run results, periods of 30 and 120 seconds were used. Figure 30 shows that the initial time period of thirty seconds causes velocity changes in the tunnel faster than the main shaft motor can adjust the radial velocity of the blades. This manifests itself in the actual velocity overshooting the target velocity resulting in an inefficient system. Figure 31 shows that the power coefficient from the test runs follows the sinusoidal schedule. The average c_p value found for the unsteady test runs was 0.291 which are higher than those for steady flow. For the 120 second period test runs, a lower average c_p value of 0.275 resulted from much noisier output signals.

Additionally, the unsteady flow results indicate that the current model in place at USAFA is not capable of modeling the rapid changes in velocity which occur in ocean waves. A motor with stronger acceleration and deceleration capabilities will need to be used to determine the effectiveness of the cycloidal propeller in real world application. However, the propeller was capable of roughly tracking the desired angular velocity, and producing mean c_p values on the order of 0.28. This provides enough evidence to support continued experimentation and evaluation of the cycloidal propeller as an energy extraction device in unsteady flow fields.

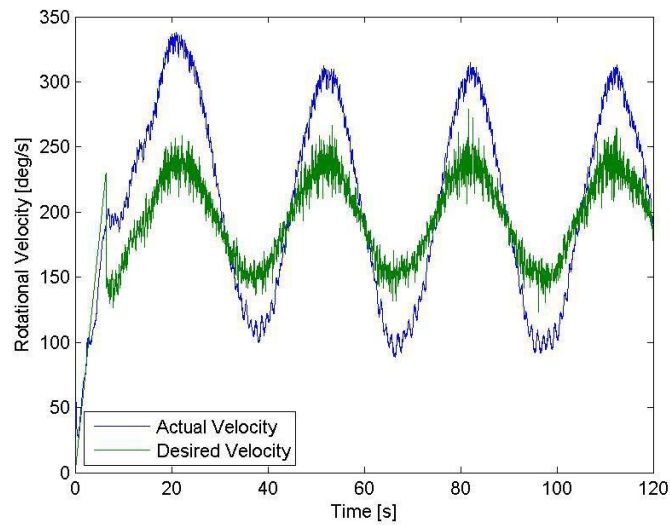


Figure 30: Main Shaft Velocity and Target Velocity vs. Time (30 second period).

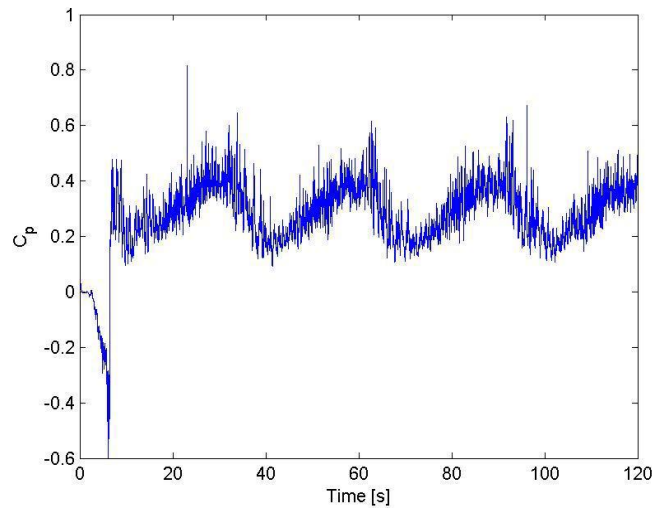


Figure 31: Power Coefficient vs. Time with 30 sec. Period.

In upcoming measurement campaigns, we plan to further investigate energy extraction using a cycloidal wave energy converter in the USAFA wave tunnel completed during year two. The wave tunnel includes a development section, test section, and dissipation section. The wavemaker (a flap hinged at the bottom of the tunnel) creates waves which are measured in the test section. The beach dissipates the waves which prevents reflection of the waves back into the test section. Initially the cycloidal wave energy converter placed in the test section will be used as a wave generator. This will allow us to independently confirm the characteristics of the wave generation as determined by the numerical simulations and in the literature. Subsequently we shall experimentally determine the cycloidal turbine energy extraction by operating the wavemaker to create waves and attempt to cancel them with the converter. In order to cancel waves we will implement the blade pitch schedules empirically determined in the water tunnel experiments as well as the feedback control algorithms. This experimental campaign for the upcoming year is a departure from the plan of performing experiments in the wave tank at Oregon State University as was initially proposed. There are many advantages of proceeding in this way. A lot more experimental runs can be performed for optimization studies because the availability of testing time will not be limited. At the Oregon State facility the budget would allow for only an approximate two week time window to perform testing. Additionally, modifications and repairs to the device will be significantly easier. Testing at the USAFA lab means the technicians who have built the device are available to us. Also the wave tank at OSU is very large and consequently the fabrication of the device and logistics of testing would be a far greater challenge. The drawback to testing in the USAFA wave tunnel is that due to the small wave height and model size the accuracy of power measurements will be limited. However, we plan to conduct more accurate power measurements under future funding, and expect all of the control algorithms developed at the small model size to be applicable to larger scale experiments.

At this point the experimental portion of the research has progressed nicely to the point where we can conduct model tests. A scale model of the cycloidal propeller has been fabricated and instrumented for

data acquisition, a flapper type wave tunnel was built and commissioned, and a flow velocity sensor and feedback controller has been calibrated. Also propeller blade pitch schedules based on flow velocity measurements have been empirically determined. All the groundwork is now in place to experimentally test the cycloidal wave energy converter in deep ocean waves, which will be accomplished in the third year of this program.

Construction of the USAFA Wave Tunnel

Figure 32 and Figure 33 show the flapper type wave maker wave tunnel constructed in year two of the project as well as the wave gauge used for calibration measurements. The wave gauge measure the change in resistance of the water caused by a change of height of the water surface as waves pass by.



Figure 32: Conceptual design of the wave tunnel and operational wave tunnel.

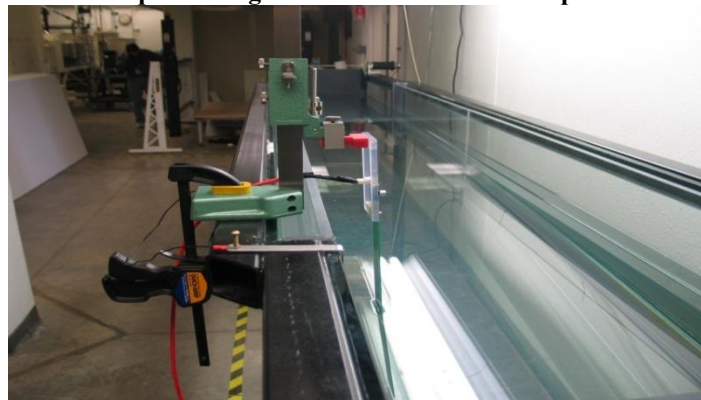


Figure 33: Wave gauge in the wave tunnel.

Cycloidal Wave Energy Converter

Figure 34: CycWEC wave tunnel model.

Simulations

While the first year was focused on simulation of deep water waves, which are numerically the easiest to model, the simulations were extended to intermediate water waves in the second year of this program. The overall numerical approach used for both types of simulations is the same, with a different governing equation for the moving vortex as shown in the following section.

Numerical Approach

A linearized potential flow formulation is used for all simulations. Potential flow is well accepted for high Reynolds number flow and provides accurate results at relatively low computational cost. This is important to be able to develop and test feedback control algorithms that are essential for the operation of the cycloidal wave energy converter. The complex velocity potential for water of finite or infinite water depth can be found in Wehausen & Laitone [19]. This potential can be used to explore the effects of water depth on the performance of the cycloidal turbine. Another objective is to model the hydrofoil as a flat plate using a vortex distribution instead of a single vortex. For this task a panel method code is implemented. This approach improves the simulation by allowing us to more accurately model the near flow field around the turbine blade. It also allows for estimates of the necessary pitching schedule to obtain the desired circulation. The flat plate simulations were run in deep water conditions.

Potential Flow Theory

For the computational simulations the fluid is assumed to be ideal. Such an assumption is valid when investigating the resulting wave patterns in the farfield sufficiently up- and down- stream of the Cycloidal turbine. Further assuming that the flow is irrotational, the velocity field, \mathbf{V} , within the domain can be represented by the gradient of a scalar potential, $\phi(x,y,z,t)$, known as the velocity potential where

$$\mathbf{V} = \nabla \phi. \quad (0.10)$$

The governing continuity equation then simplifies to the Laplace equation,

$$\nabla^2 \phi = 0, \quad (0.11)$$

and must hold throughout the fluid.

In addition, for two-dimensional planar flow, continuity dictates that the velocity components in the x and y directions respectively, (u, v) , can be expressed in terms of the stream function $\psi(x,y,t)$, which relates to the velocities as,

$$u = \frac{\partial \psi}{\partial y}, \quad v = -\frac{\partial \psi}{\partial x}. \quad (0.12)$$

For two-dimensional planar flows it is often convenient to represent the velocity field as analytic functions of a complex variable. Assuming the flow depends only on the x and y spatial coordinates which are taken as the real and imaginary parts of the complex variable $z = x + iy$, and time, t , one can define the complex potential $F(z, t)$ to be

$$F(z, t) = \varphi + i\psi \quad (0.13)$$

The real and imaginary components of F must satisfy the Cauchy-Riemann equations and therefore its derivative is

$$\frac{\partial F}{\partial z} = u - iv \quad (0.14)$$

For ideal flow the conservation of momentum leads to the well-known Euler equations. The Euler equations can be integrated resulting in an explicit equation for the pressure field known as the Bernoulli equation. For two-dimensional irrotational flow, the unsteady Bernoulli equation can be expressed in terms of the potential function as follows,

$$\frac{\partial \varphi}{\partial t} + \frac{1}{2} \left(\left(\frac{\partial \varphi}{\partial x} \right)^2 + \left(\frac{\partial \varphi}{\partial y} \right)^2 \right) + \frac{p}{\rho} + gy = C \quad (0.15)$$

where the spatial coordinate y is in the direction of the gravitational field g .

Linearized Free Surface Boundary Condition

Unique solutions for φ and ψ are determined by satisfying Equations 0.14 and 0.15 and the appropriate boundary conditions. At the upwave and downwave integration boundaries, the waves within the domain are allowed to freely leave the domain. For the current flow field of critical importance is the free surface boundary condition. A detailed development of the linearized free surface boundary condition can be found in Newman [1999] and only a brief summary is presented here.

At the free surface both the kinematic and dynamic boundary conditions must be satisfied. The kinematic boundary condition states that there shall be no flow across the interface at the free surface and the dynamic boundary condition states that the pressure on the free surface must be atmospheric. A Cartesian coordinate operating system is defined such that $y = 0$ is the location of the undisturbed free surface and the y -axis points upwards. We also define the free surface elevation at any given horizontal location as $\eta(x, t)$. The kinematic boundary condition requires the substantial derivative of the quantity $y - \eta$ equals 0 on the free surface. Neglecting higher order terms, the result is

$$\frac{\partial \eta}{\partial t} = \frac{\partial \varphi}{\partial y} \quad (0.16)$$

which states that the vertical velocity of the free surface and the fluid are equal.

The dynamic boundary condition is determined from Bernoulli's equation 0.15 above. Assuming constant atmospheric pressure on the surface, substituting the free surface elevation for y , and again neglecting higher order terms results in

$$\eta = -g \frac{\partial \phi}{\partial t}, \quad (0.17)$$

which, due to the linearization can be imposed at $y = 0$.

Potential Vortex under a Free Surface in Infinite Depth Water

The complex potential for a vortex moving under a free surface with position $c(t)$ in the complex plane is developed in Wehausen & Laitone (1960) to be

$$F(z, t) = \frac{\Gamma}{2\pi i} \ln \left(\frac{z - c(t)}{z - \bar{c}(t)} \right) + \frac{g}{\pi i} \int_0^\infty \int_0^\infty \frac{\Gamma}{\sqrt{gk}} e^{-ik\bar{c}(t)} e^{-\tau} \sin(\sqrt{gk}(t - \tau)) d\tau dk. \quad (0.18)$$

Equation 0.18 satisfies both the kinematic and dynamic free surface boundary conditions at $y = 0$. The first term is the complex potential due to the vortex and its image, which is necessary to satisfy the kinematic free surface condition. The second term describes the radiated waves related to the dynamic free surface condition. It is also important to note that in Equation 0.15 the fluid is assumed to be infinitely deep.

Bottom Boundary Condition

In addition to the free surface boundary condition the potential must satisfy the no flow boundary condition

$$\frac{\partial \phi}{\partial y} = 0, \quad (0.19)$$

at the ocean floor, $y = -D$.

Potential Vortex under a Free Surface in Finite Depth Water

The complex potential for a vortex moving under a free surface with position $c(t)$ in the complex plane is developed in Wehausen & Laitone (1960) to be

$$\begin{aligned}
F(x, t) = & \frac{\Gamma}{2\pi i} \ln(x - c(t)) - \frac{\Gamma}{2\pi i} \ln(x - \bar{c}(t) + 2iD) \\
& + \frac{\Gamma}{\pi} \int_0^\infty \frac{e^{-kD}}{k \cosh(kD)} \times \sinh(b(t) + D) \sin(k(z - a(t) + iD)) dk \\
& - \frac{g}{\pi i} \int_b^\infty \frac{\text{sech}^2(kD)}{\sqrt{gk \tanh(kD)}} dk \times \int_0^t \Gamma(\tau) \sinh(k(b(\tau) + D) \sin(k(z - a(\tau) + iD)) \\
& \times \sin[\sqrt{gk \tanh(kD)}(t - \tau)] d\tau
\end{aligned}
\tag{0.20}$$

where $\Gamma(t)$ is the circulation of the vortex, $g=9.81 \text{ ms}^{-2}$ the gravity constant, and k the wave number. Equation 0.20 satisfies both the kinematic and dynamic free surface boundary conditions at $y = 0$ and the bottom boundary condition at $y = -D$. The first and second terms are the complex potential due to the vortex and its image, which is necessary to satisfy the kinematic free surface condition. The additional term describes the radiated waves related to the dynamic free surface condition.

Computational Setup

The position of the vortex is prescribed as a function of time. The coordinates for the vortex moving about the center of rotation $(0, y_c)$ with radius R and frequency ω are

$$\begin{aligned}
c_x(t) &= R \cos(\omega_c t + \theta) \\
c_y(t) &= y_c - R \sin(\omega_c t + \theta)
\end{aligned}
\tag{0.21}$$

An arbitrary phase shift θ is introduced, which indicates the relative phase between an incoming Airy wave and the cycloidal wave energy converter motion. Experiments conducted by Pinkster and Hermans (1990) showed that the cycloidal propeller is a naturally stable rotating system that automatically synchronizes itself to the rotational frequency of an incoming wave. While we do not rely on this self-synchronization capability in the present investigation, we limit ourselves to operation of the cycloidal propeller at the same rotational frequency ω_c as that of the incoming Airy wave:

$$\omega_c = \omega_{\text{Airy}} \tag{0.22}$$

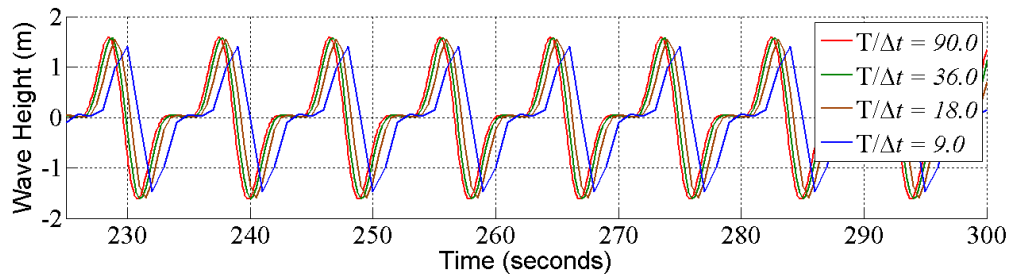
Therefore, ω is defined by the incoming wave from which energy is to be extracted and the only independent variables in Equation 0.22 are R and y_c . Modeling the motion of the turbine blades in this fashion syncs the blades to the orbital motion of the fluid particles. This is appropriate for deep water and valid in intermediate water depths. For shallower water the particle orbits become more and more elliptical with decreasing water depth and the synchronization will need further examination.

Results Deep Water Simulations

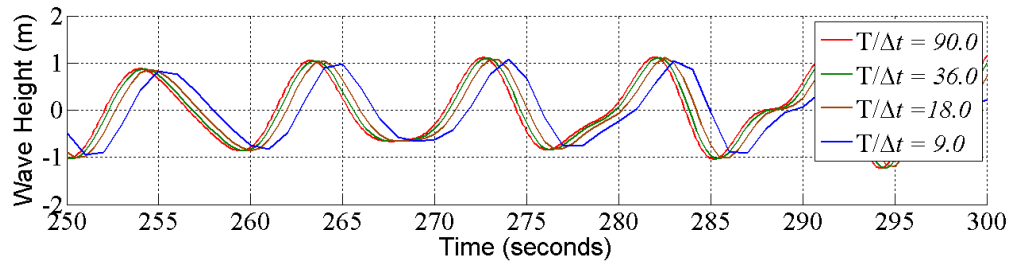
Resolution Study

For all of the simulations it is imperative to ensure that the time step and wave number integration settings are such that the solution converges. In this section resulting wave patterns are presented as a function of Δt , Δk , and k_{max} to determine appropriate values for each variable. All results are normalized relative to a standard north Atlantic deep ocean wave which has a wave length $\lambda = 126.5$ m, wave number $k = 1/\lambda$, amplitude $A_p = 1.75$ m and period $T = 9$ seconds. Results are plotted at constant horizontal location, in particular, at $x=126.5$ and 1012 m, which correspond to $\lambda = 1$ and 8 wavelengths downwave from the Cycloidal wave energy converter.

The effect of varying Δt is shown in Figure 35 with constant $k/\Delta k = 31.6$ and $k_{max}/k = 75.9$. These plots show a phase shift as Δt increases. In addition, for $T/\Delta t = 9.0$ the maximum wave amplitude is incorrect or possibly missed due to insufficient resolution of Δt . From these results it was concluded that the proper time step for these simulations is $T/\Delta t = 36$, which states that there should be 36 azimuthal locations calculated for each revolution of the Cycloidal wave energy converter.



(a) $x = \lambda$.



(b) $x = 8\lambda$.

Figure 35 The effect of Δt on the generated wave with $k/\Delta k = 31.6$, $k_{max}/k = 75.9$.

The effect of varying Δk is shown in Figure 36 with constant $T/\Delta t = 36.0$ and $k_{max}/k = 75.9$. These plots show that a $k/\Delta k = 31.6$ is required for independence at both horizontal locations. Physically this can be interpreted as requiring a step size for the integral over the wave number that is 31.6 times smaller than the wave number of the first harmonic generated by the Cycloidal wave energy converter.

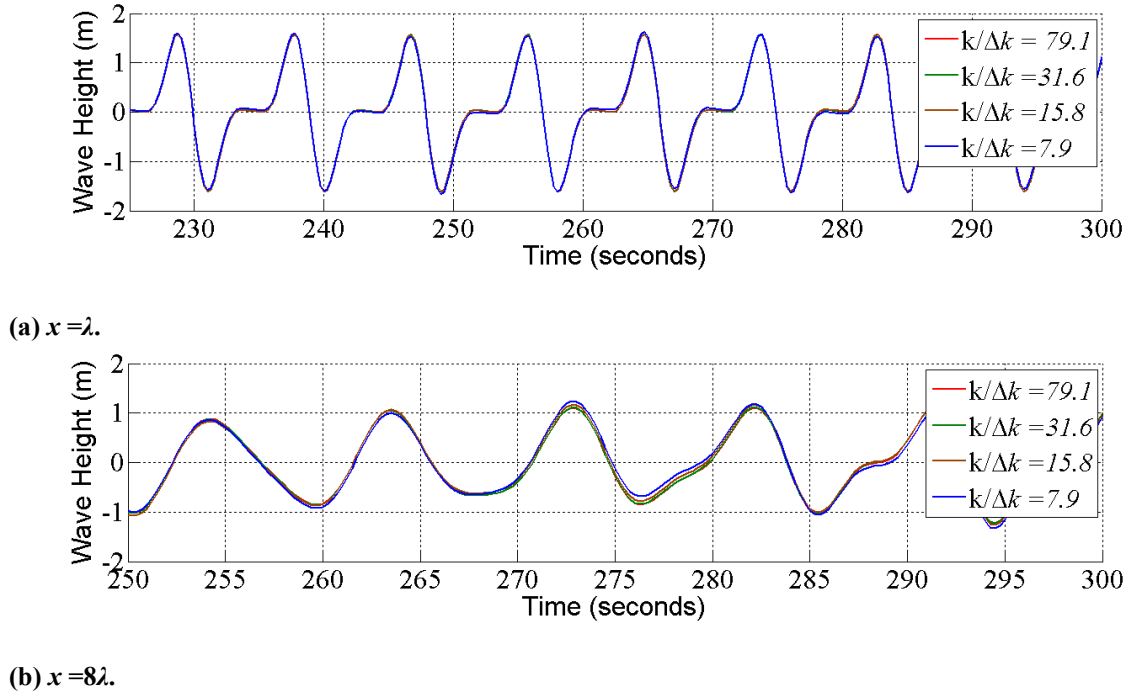
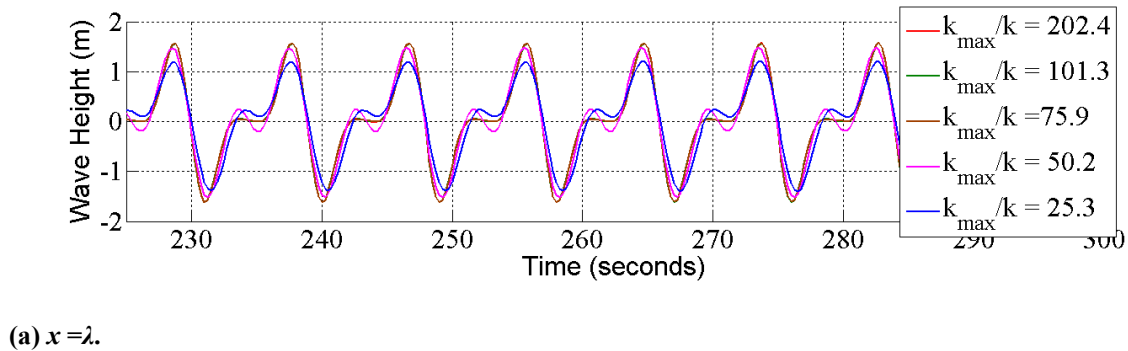
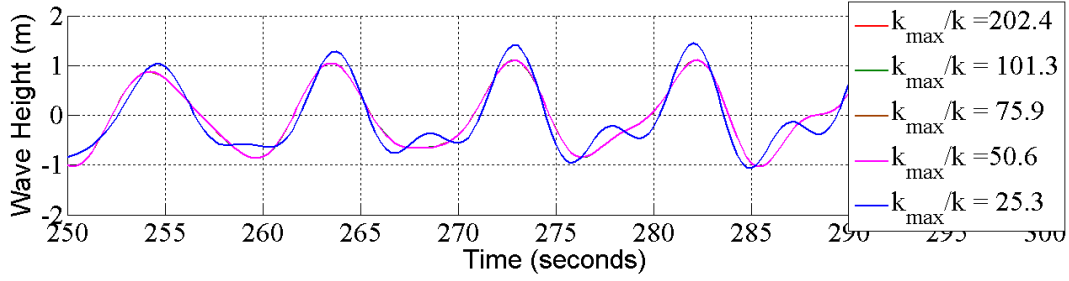


Figure 36 The effect of Δk on the generated wave with $T/\Delta t = 36$ and $k_{max}/k = 75.9$.

The effect of varying k_{max} is shown in Figure 37 with constant $T/\Delta t = 36.0$ and $k/\Delta k = 31.6$. These plots show that $k_{max}/k = 75.9$ is required for independence at both horizontal locations. Using the Nyquist sampling theory this can be interpreted as requiring the radiated effects for all waves with wave lengths greater than 3.2 m. Given that the first harmonic generated by the Cycloidal wave energy converter has a wave length equal to 126.5 m is would appear reasonable to neglect the effects of radiated waves with wave lengths less than 3.2 m.

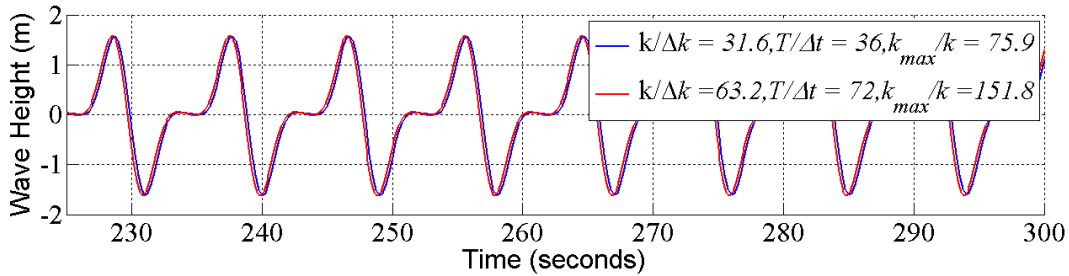




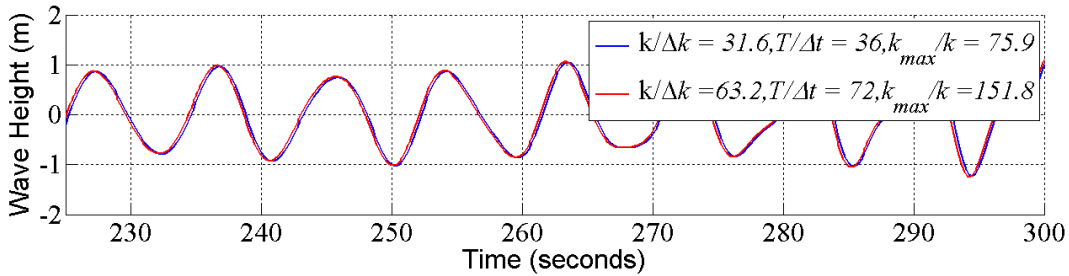
(b) $x=8\lambda$.

Figure 37 The effect of k_{max} on the generated wave with $T/\Delta t=36$ and $k/\Delta k = 31.6$.

Based on the above results it was concluded that the required settings for numerical convergence are $T/\Delta t=36$, $k/\Delta k = 31.6$, and $k_{max}/k = 75.9$. Shown below in Figure 38 is a comparison of generated waves using these integration settings and twice the resolution in time, wave number increment and maximum wave number. Results are again shown for $x = \lambda$ and 8λ . Both simulations predict nearly identical wave patterns indicating that the chosen settings are sufficient, thus we use them in all results presented as standard settings.



(a) $x=\lambda$.



(b) $x=8\lambda$.

Figure 38 A comparison of chosen standard integration settings to twice the time step, maximum wave number and half the wave number integration step.

Single Vortex Simulations

Results from single vortex simulations, representing a single bladed Cycloidal wave energy converter are presented in this section. The goal of these simulations is to investigate the nature of the waves generated by the Cycloidal wave energy converter and to determine optimal values for the centroid location beneath the water surface y_c , the wave energy converter radius R , and the circulation Γ , which in turn, determines the required chord length and lift coefficient of the hydrofoil. The desired wave pattern in these simulations is one where there is a downwave travelling wave at the fundamental frequency, with no higher frequency waves present. In the upwave direction, no waves should be shed. A wave pattern of this type can be used to perfectly cancel an incoming wave of the fundamental frequency, thus allowing for extraction of all power present in this wave. Any additional waves shed upwave or downwave will reduce the efficiency of the wave termination scheme.

Plotted in Figure 39 are resulting wave elevations downwave of the Cycloidal wave energy converter at a constant horizontal position $x = 3\lambda$. The center of rotation, y_c , is varied while the radius $R = 12$ m and circulation $\Gamma = 22.5$ m/s are kept constant. The resulting wave patterns are clearly a function of y_c , and as the results in this section will highlight, are also a function of R and Γ . Fourier analysis of the resulting wave patterns show that all patterns primarily consist of the first three harmonics, with the first harmonic having a frequency equal to the rotational period of the Cycloidal wave energy converter and wave length of 126.5 m. The primary difference between all of the wave patterns is the amplitude of each harmonic.

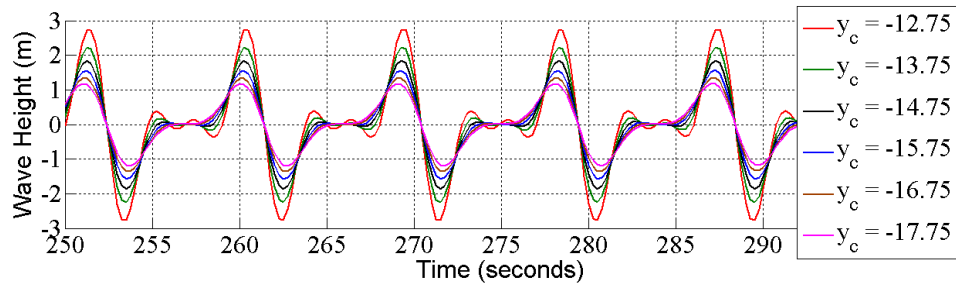
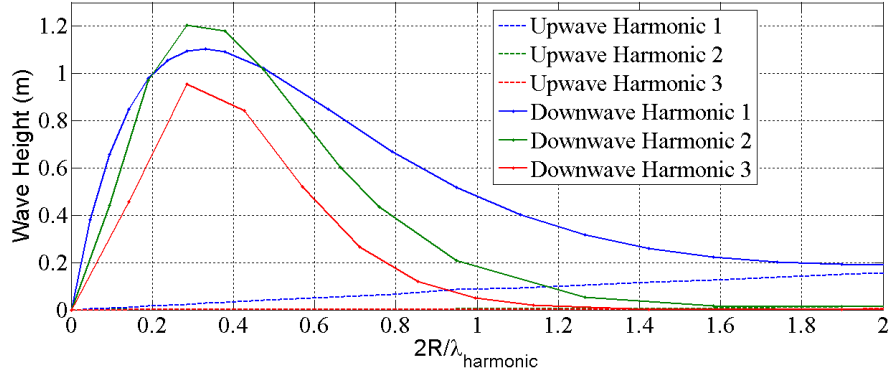
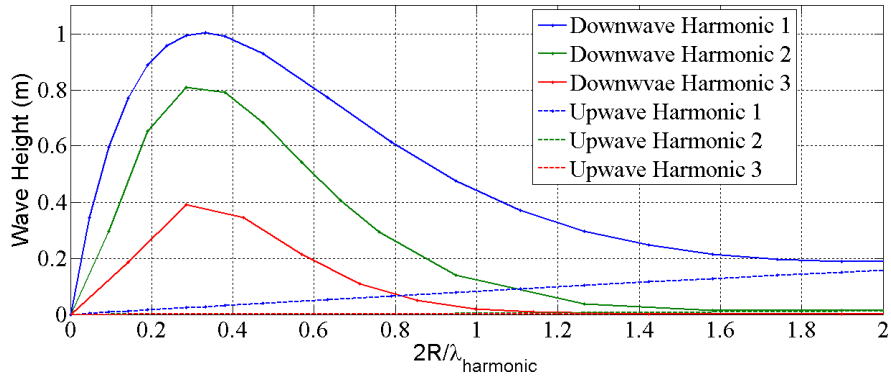


Figure 39 Simulated wave patterns at $x = 3\lambda$ as a function of y_c for $\Gamma = 22.5$ m²/s and $R = 12$ m.

To determine the effect of varying the Cycloidal wave energy converter radius on the resulting wave patterns, simulations were completed with constant circulation and constant y_{min} , where $y_{min} = -y_c - R$. Plotted in Figure 40 are wave amplitudes downwave and upwave at $x = \pm 3\lambda$ for each of the first three harmonics, which were determined using Fourier analysis. The results are plotted as a function of $2R/\lambda_{harmonic}$, where $\lambda_{harmonic}$ is the wave length of the corresponding harmonic. Results are shown for $y_{min} = 3.75$ and 1.75 m, respectively. Notice that for all cases downwave, i.e. $x = 3\lambda$, the wave amplitude increases to a maximum value before decreasing for larger radii. The maximum occurs at the same value of $2R/\lambda_{harmonic} = 0.33$ independent of the wave energy converter center location. For a wave length of 126.5 m the maximum amplitude for the first harmonic occurs when $R = 21.75$ m. It is also important to note that as y_{min} was increased from 1.75 m to 3.75 m the amplitudes of the second and third harmonics decreased at a faster rate than the first harmonic. Upwave at $x = -3\lambda$ the resulting wave pattern primarily consists of the first harmonic. Its amplitude increases nearly linearly with increasing radius and for most practical values of $2R/\lambda_{harmonic}$ the amplitude is relatively insignificant.



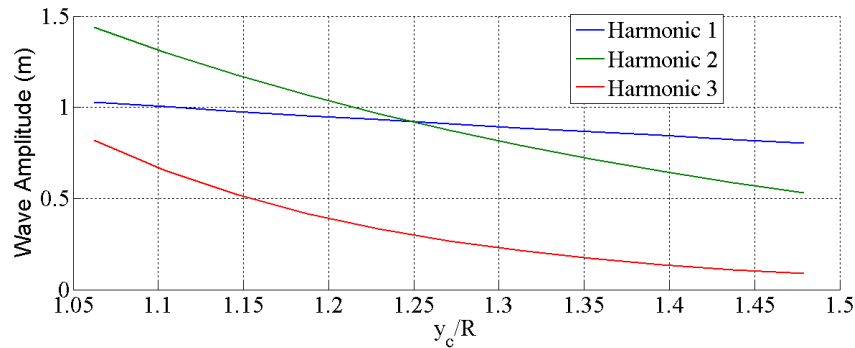
(a) $y_{\min} = 1.75$ m.



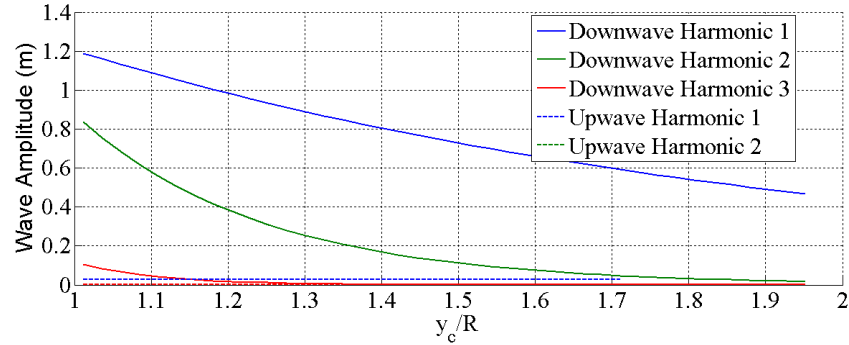
(b) $y_{\min} = 3.75$ m.

Figure 40 Wave amplitude for each of the 1st three harmonics as a function of R for $y_{\min} = 1.75$ and 3.75 m.

To determine the effect of varying the depth of the Cycloidal wave energy converter beneath the water surface on the resulting wave pattern, simulations were completed with constant circulation and constant radius but with varying y_c . Plotted in Figure 41 are wave amplitudes at $x = \pm 3\lambda$ for each of the first three harmonics, which were again determined using Fourier analysis. The results are plotted as a function of y_c/R . Results are shown for the downwave location only at $2R/\lambda = 0.189$ and for both the upwave and downwave locations for $2R/\lambda = 0.328$. These results show a linear decrease in the amplitude of the first harmonic as y_c is increased, while the second and third harmonics experience an exponential decrease.



(a) $2R/\lambda = 0.189$.



(b) $2R/\lambda = 0.328$.

Figure 41 Wave amplitude for each of the first three harmonics as a function of y_c/R . Results are shown for $2R/\lambda = 0.189$ and 0.328 .

To determine the effect of varying the circulation strength on the resulting wave pattern, simulations were completed with constant y_c and radius but with varying Γ . Plotted in Figure 42 is the wave amplitude of the first three harmonics at $x=3\lambda$ as a function of Γ for $y_c = 15.75$ and $R = 12$. As expected from Equation 0.22, the results clearly show a linear relationship between Γ and wave amplitude for all three harmonics. The implication of this result is that once the optimal values for y_c and R have been determined the circulation can be adjusted accordingly to achieve the desired wave amplitude.

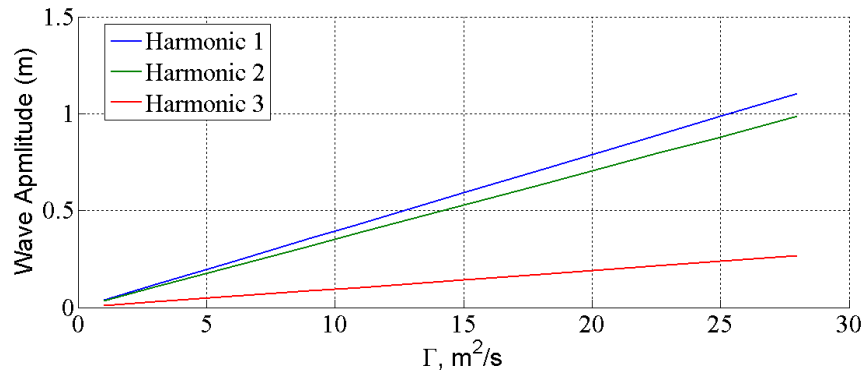


Figure 42 Wave amplitude for each of the first three harmonics as a function of Γ for $y_c = 15.75$ m, $R = 12$ m.

Multi-Vortex Simulations

Using the theory of superposition is it possible to combine the velocity potential from single vortex simulations to represent a multi-bladed Cycloidal wave energy converter. Results are shown in this section for simulations with two vortices with 180° of phase shift and equal but opposite circulation.

Plotted in Figure 43 are the amplitudes of the first three harmonics for each vortex and for the combined resulting wave pattern. It is important to note that the first harmonic waves from each vortex combines to produce a wave with twice the amplitude of each vortex separately. In addition, the second harmonic waves from each vortex cancel each other entirely. The third harmonic waves also combines to produce a wave with twice the amplitude but with suitable choices of y_c and R the energy content of the resulting wave is relatively insignificant.

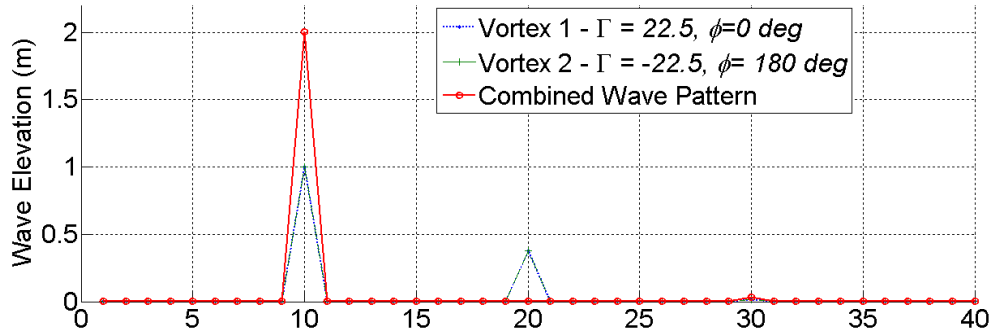


Figure 43 Wave amplitude for each of the first three harmonics for two vortices of equal but opposite circulation and with 180° phase along with the harmonics of the combined wave pattern.

Plotted in Figure 44 are the resulting wave patterns at $x = 3\lambda$ for each individual vortex and for the combined vortex pair. It is important to note that the combined wave pattern primarily consists of the first harmonic with a period of $T = 9$ seconds and wave length $\lambda = 126.5$ m. The implication of this result is that if the Cycloidal wave energy converter is in the correct phase with an incoming deep ocean wave, this wave can be almost completely cancelled downwave of the cycloidal turbine, thereby extracting nearly all of the energy from the incoming wave.

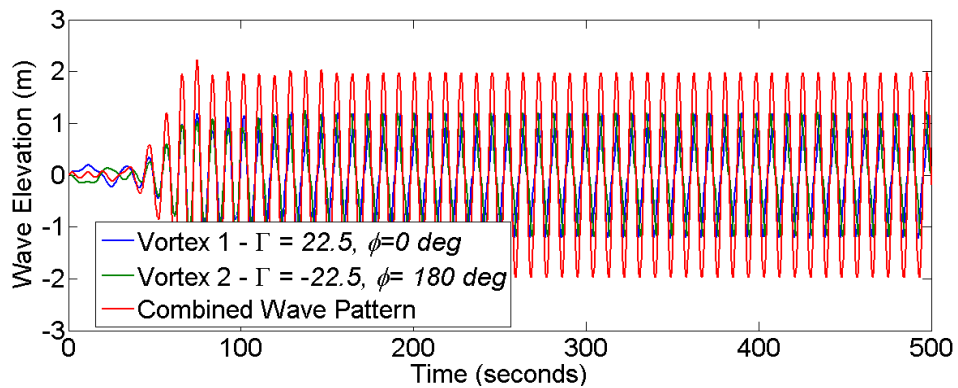


Figure 44 Simulated wave patterns at $x = 3\lambda$ for two vortices of equal but opposite circulation and with 180° phase along with the wave pattern of the combined vortex system.

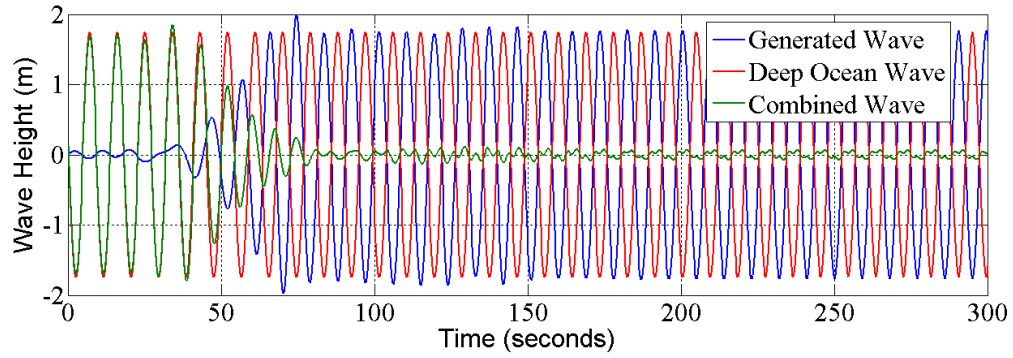
Wave Cancellation

Further extending the principle of superposition it is possible to combine the complex velocity potential of an Airy linear deep ocean wave with that of the multi-vortex simulations representing the Cycloidal turbine to determine the resulting wave pattern caused by the interaction of the Airy wave and the turbine. The velocity potential for a progressive linear deep ocean wave is given in Newman (1999) to be

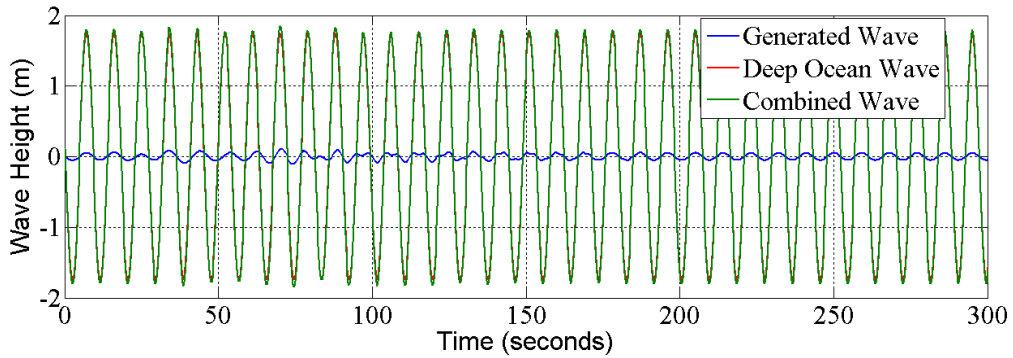
$$\phi(x, y, t) = \frac{A_p g}{\omega} e^{ky} \sin(x - \omega t + \vartheta) \quad (0.23)$$

where A_p is the wave amplitude, ω is the wave frequency, k is the wave number and ϑ is an arbitrary phase shift.

Plotted below in Figure 45 is the wave pattern for a deep ocean wave as a function of time at a constant axial locations of $x = \pm 3\lambda$. The wave amplitude is 1.75 m and the period is 9 seconds. Using deep ocean wave theory it is possible to show that the wave length is $\lambda = 126.5$ m and the power convected by the wave is 108 kW per meter of wave crest. Also shown in Figure 45 is the resulting wave pattern from a two-vortex simulation with $R = 21.75$ m, $y_c = 25.5$ m and $\Gamma = \pm 20.2$ m²/s, and the combined wave pattern due to both the incoming wave and the waves shed by the Cycloidal wave energy converter. As seen in Figure 45, downwave of the Cycloidal wave energy converter the amplitude of the combined wave pattern has been reduced by 96% compared to the incoming deep ocean wave, while upwave the combined wave pattern is nearly identical to the incoming deep ocean wave. Using control volume analysis, the implication of this result is that over 96% of the 108kW of power per meter depth of wave crest of the incoming wave has been extracted by the Cycloidal wave energy converter. This is a very promising result that highlights the Cycloidal turbine's ability to efficiently extract large amounts of energy. Given the energy per meter of wave crest, it would be possible to construct a Cycloidal turbine wave energy converter plant that delivers power comparable in magnitude to existing conventional power plants. For example, a total length in the crest direction of 1000m total would allow extraction of about 100MW of electric power. It is also worth noting that there will be further losses due to three dimensional as well as viscous flow effects, as well as mechanical and electrical efficiencies that we plan to quantify in our continuing research. However, the results presented here for inviscid two-dimensional flow exceed by far all other wave energy converters known to the authors that are currently being developed or considered in terms of efficiency.



(a) $x = 3\lambda$.



(b) $x = -3\lambda$.

Figure 45 Simulated wave patterns at $x = \pm 3\lambda$ for a two bladed Cycloidal wave energy converter and an incoming deep ocean wave.

Results Intermediate Water Simulations

It is convenient to view the wave energy converter as a wave generator producing anti-waves to the incoming waves which, when superimposed, cancel out the waves. For the initial results we will show the performance of the cycloidal propeller both as an efficient wave maker as well as a wave termination device for intermediate ocean waves. We show inviscid two dimensional simulation results for a cycloidal wave energy converter featuring both a single blade as well as two blades spaced 180° apart. In these simulations, the blades of the wave energy converter are modeled as a point vortex. For wave generation, we find that it is possible to create a single Airy type wave that only travels in one direction, with no wave being generated in the other direction. The direction of travel is controlled by the rotation direction. This is shown in Figure 46. Figure 47 shows the water surface time history at $\pm 3\lambda$.

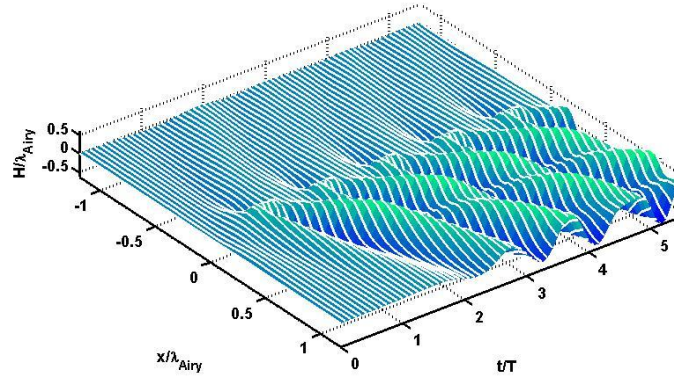


Figure 46: Wave height for wave generation using a single bladed wave energy converter.
All waves evaluated at $x = \pm 3\lambda$.

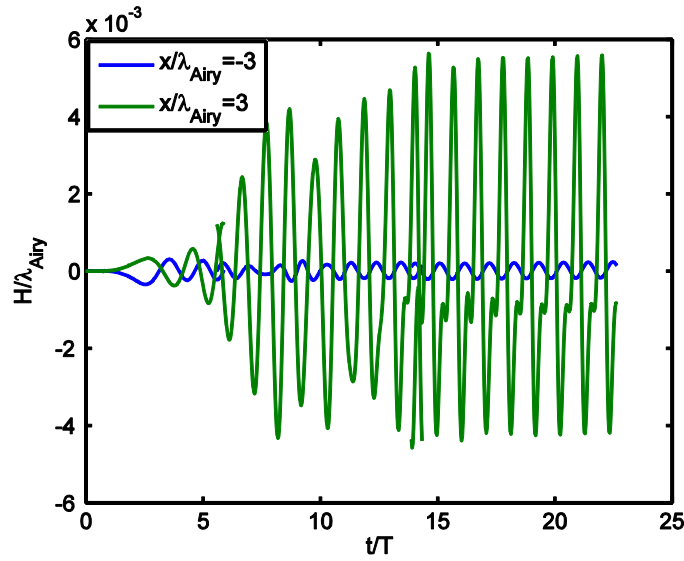


Figure 47: Wave Height of the Up-wave and Down-wave at $x = \pm 3\lambda$.

Depending on geometry choices for converter radius and submergence depth, in addition to the fundamental wave traveling in one direction, up to two higher harmonic waves traveling up and downwave can be observed. This is shown in the power spectral density plot of Figure 48.

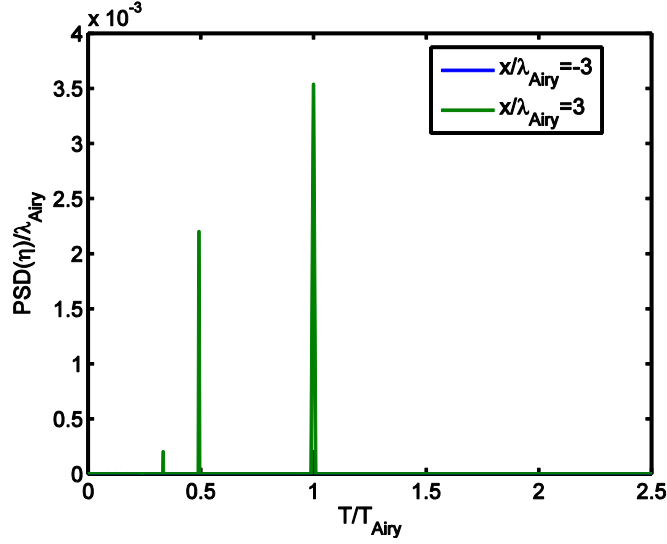


Figure 48: Power Spectral Density of the surface at $x = \pm 3\lambda$.

A parameter study investigating the impact of wave energy converter size shows that the largest amplitude fundamental wave is obtained for a device of size $2R/\lambda_{Airy} = 1/\pi$. This size corresponds to an exact match between the rotational velocity of the hydrofoil and the wave velocity. In this study the circulation and submergence level were kept constant. Shown in Figure 49 are wave amplitudes up-wave and down-wave at $x = \pm 3\lambda$ for each of the first three harmonics determined using power spectral analysis. Clearly there is a maximum of the amplitude of the fundamental wave traveling down-wave, H_1 at a size of $2R/\lambda_{Airy} = 0.32$.

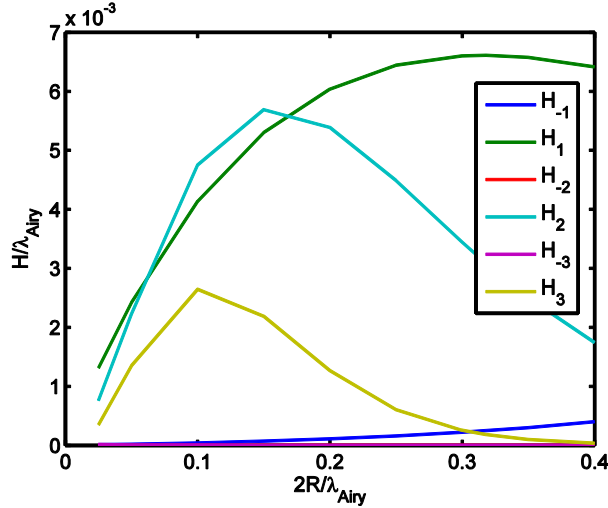


Figure 49: Wave height for different size radius cycloidal wave energy converter for fixed circulation and submergence. All waves evaluated at $x = 3\lambda$.

Another parameter study was conducted to investigate the effect of submergence depth. Results of this are shown in Figure 50. An interesting result is that as the cycloidal wave energy converter is moved closer to the ocean floor, an increase in the amplitude of the fundamental wave traveling upwave is seen. This result is a marked difference from deep water results that do not show this effect.

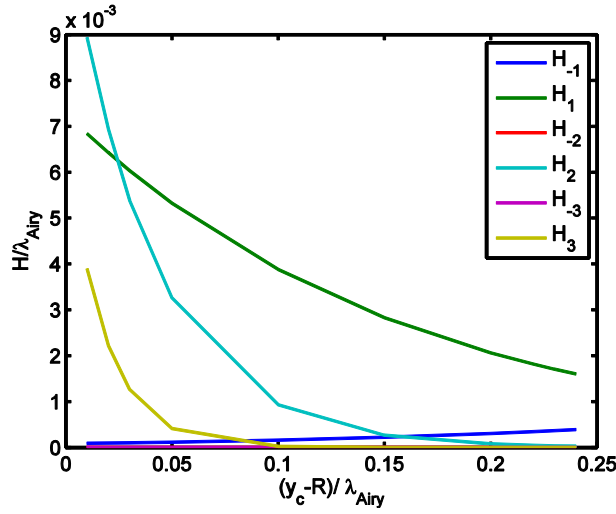


Figure 50: Wave height for different submergence depths.

The single sided wave generated by the cycloidal wave energy converter is perfectly suited to extract energy from an incoming plane Airy wave. In order to achieve this, the motion of the wave energy converter needs to be synchronized in frequency and phase locked to the incoming wave using feedback control, and the circulation of the converter's hydrofoils needs to be adjusted to produce a wave of matching amplitude. We employ the following linear feedback laws:

$$\begin{aligned}\delta(t) &= \omega t + \theta \\ \Gamma &= k_{\Gamma} H_{\text{Airy}}\end{aligned}$$

(0.24)

Where $\delta(t)$ is the angle of the cycloidal wave energy converter main shaft, and θ is a constant phase shift between the wave motion and the converter rotational angle. The fixed feedback gain k_{Γ} is adjusted such that the amplitude of the wave H_1 created by the wave energy converter matches that of the incoming Airy wave exactly. If this is accomplished more than 95% of the incoming wave energy can be extracted from the wave effectively terminating the wave. This is shown in Figure 51 which shows the time history of the water surface downstream of the energy converter.

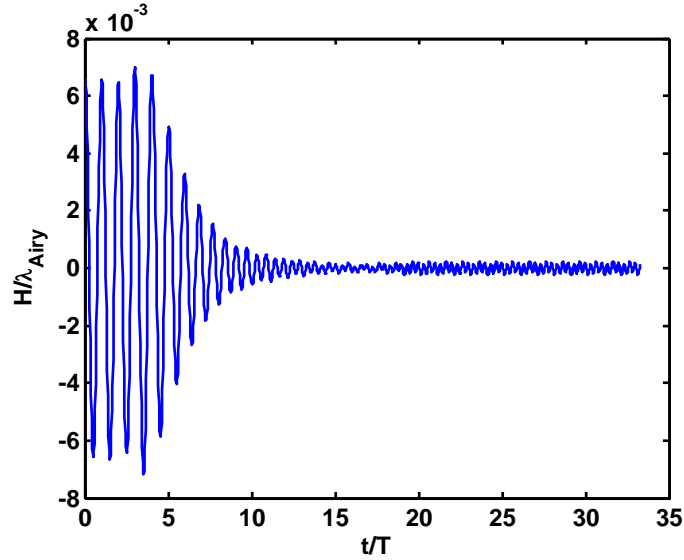


Figure 51: Wave height for a feedback phase of $\theta = 10^\circ$ of the cycloidal WEC with two vortices spaced 180° apart.

Flat Plate Simulations

To model the hydrofoil as a zero thickness flat plate a vortex panel code was written that includes the effects of the free surface. In this simulation the hydrofoil is modeled as a distribution of vortices. In addition, the no-flow through boundary condition must be satisfied along the flat plate and Kelvin's circulation theorem can be used to model the wake. An important initial step to validate the flat panel code is the comparison of the far field wave pattern created by the flat panel simulation to the results obtained from single vortex simulations. For small chord length to wavelength ratios, the results from the flat plate simulations are expected to match those obtained with the single vortex representation of the flow. Figure 29 (upper right) shows this comparison where the panel circulation was fixed to match the single vortex circulation of $\Gamma = 10$. Figure 52 (lower left) shows the comparison for a fixed pitch angle of 7.4° which is the average pitch angle of the constant circulation case which is shown in Figure 52 (lower right). Clearly the results show very good agreement. Clearly it can be observed that the overall deviation from the mean pitch angle is small in the constant circulation case and deviation from the constant circulation value is small in the constant pitch angle case. This indicates that the wave induced flow field direction and magnitude do not change significantly as the hydrofoil travels on its circular path which is to be expected, to first order. The reason for the observed deviations is the relative size of the wave energy converter in comparison to the wave length, which at a diameter of half a wavelength cannot be considered small in the case shown.

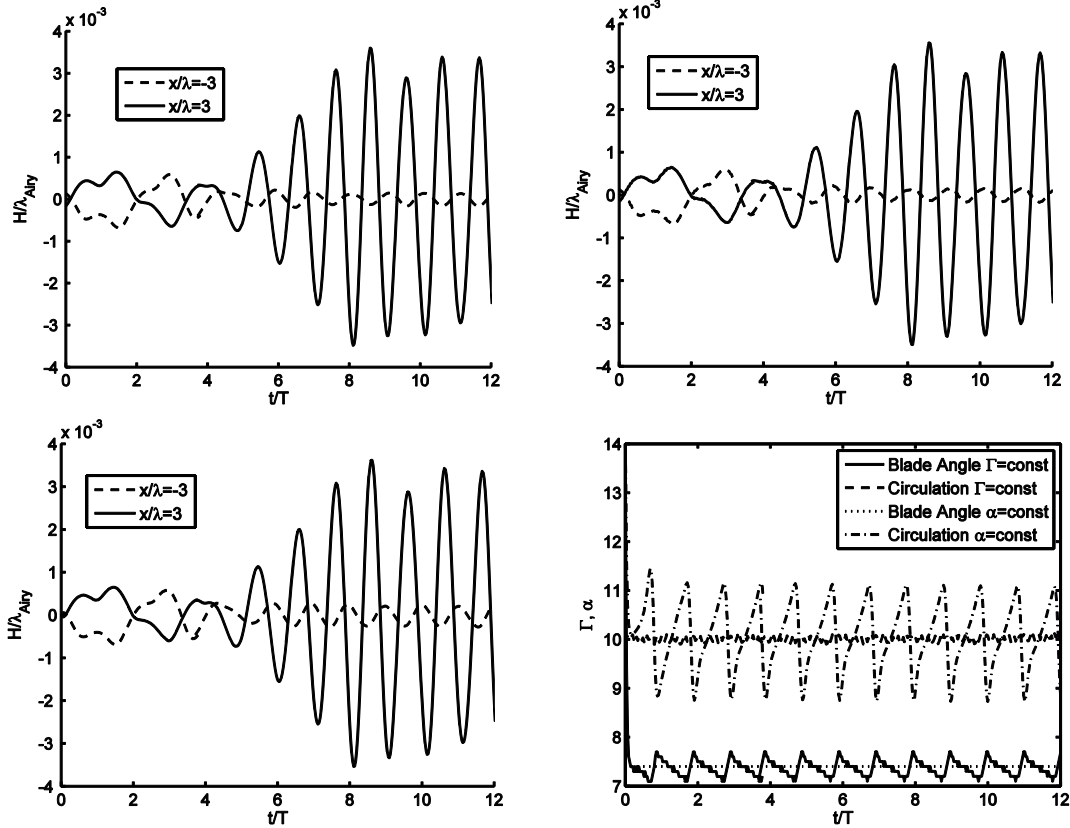


Figure 52: Comparison of the single vortex (top left), flat plate with constant circulation (top right), and flat plate with constant pitch angle (bottom left).

The flat plate representation of the wave energy converter hydrofoil allows for investigation of the impact of the plate chord length on the waves created. This is shown in Figure 53. As the chord length increases, the height of the fundamental wave generated increase even though the plate circulation was kept constant at $\Gamma = 10$ for all the different simulations. Also evident from the right hand plot in Figure 30 is the larger change in blade pitch angle which is needed to compensate for the effect of apparent camber as the chord length increases. The increase in wave height is attributed to the fact that a larger chord close to the surface will be able to more effectively change the surface and thus create a wave even at the same circulation.

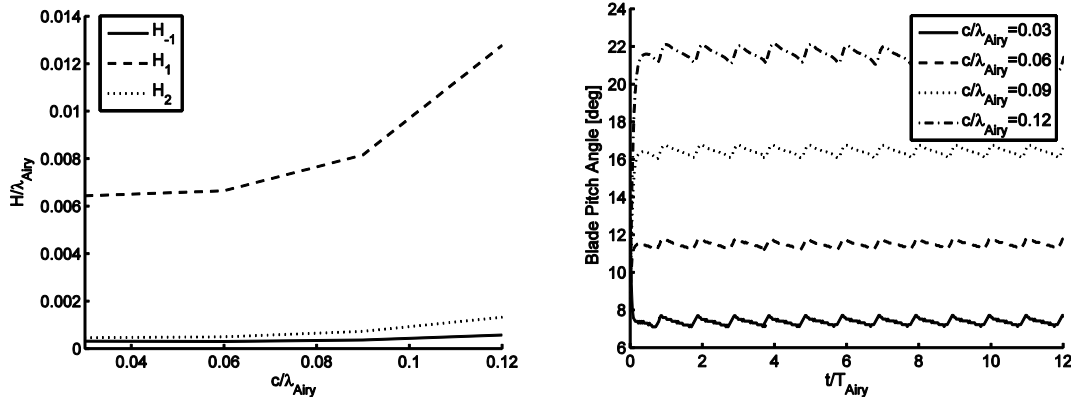


Figure 53: Impact of chord length on wave generation (left), corresponding pitch angles (right).

The cancellation of incoming waves by using a flat plate model of the wave energy converter hydrofoils was also investigated. The main benefit of the flat plate simulation lies in the physically correct modeling of the blade pitch angle, which is an important consideration for experimental and real life implementations.

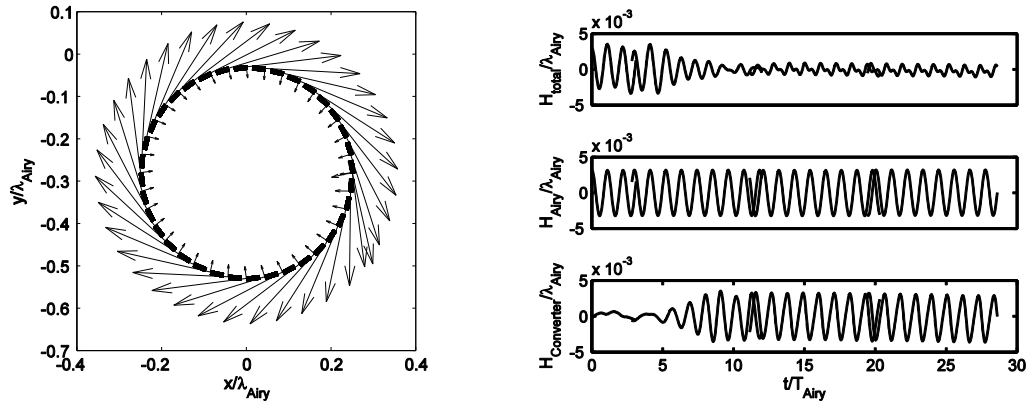


Figure 54: Radial and tangential velocity components (left), surface at $x = 3\lambda$ (right) for interaction of a single bladed cycloidal wave energy converter and an incoming wave at phase $\theta = 0$ and equal amplitude.

Figure 54 (right) shows the cancellation of an incoming wave. The bottom plot shows the time history of the water surface at $x = 3\lambda$ for the flat plate generated wave, the middle plot shows the incoming wave time history at $x = 3\lambda$, and the top plot shows the superposition those two. Interestingly, the left side of Figure 31 shows the tangential and normal components of the blade velocity as the blade rotates its first full rotation. Aside from the startup the velocity components resulting from the interaction of the converter and wave field lead to a mostly constant inflow to the blade throughout the entire rotation. This is important for generator design because, as a consequence, the torque and shaft power produced are also constant in time. Thus by operating the cycloidal wave energy converter in sync with the waves, not only is the incoming wave cancelled but the fluctuating velocity field is rectified to achieve an almost constant inflow at the blade.

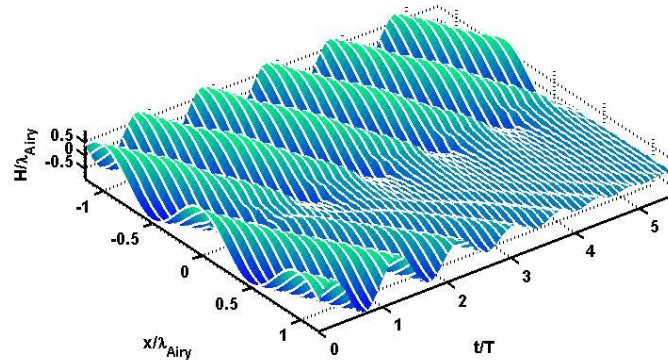


Figure 55: Water surface time plot for wave cancellation of an Airy wave travelling in the positive x direction using a single flat plate cycloidal wave energy converter.

The same simulation as for Figure 54 is also shown in Figure 55 where the temporal evolution of the wave cancellation can be seen. For the cancellation to be effective in the spatial domain shown, about 5 wave periods are necessary.

At this point in the computational portion on the research we have shown great potential to extract a significant fraction of the energy available from waves. This is true for deep water ocean waves and intermediate depth waves. Indeed much of the results for intermediate depth runs were the same as those for deep water runs, including termination of 95% of the incoming wave energy. One interesting difference for intermediate waves was the amplitude of the up-wave grew as the device submergence increased. This was not seen in deep water studies. Modeling of the hydrofoil was performed using a distribution of vortices. The far field properties matched those for single vortices as expected. The impact of plate chord length on the waves created was investigated. The fundamental wave height was shown to increase for longer chord even as circulation was kept constant likely due to the blade being closer to the surface. Also a larger blade pitch angle is needed to compensate for apparent camber as chord length increases.

Cadet and Faculty / Researcher involvement

As the involvement of Air Force Academy Cadets as well as Researchers, Graduate Students and Postdoctoral as well as Visiting Researchers was explicitly spelled out as a task in the Statement of Objectives, this section summarizes all parties involved in this work to date. In the overall flow of daily work, a significant portion of my time was spent mentoring and advising. On the other hand, without the contributions of all of these outstanding individuals, the project could not have achieved the results that it has achieved to date.

With the funding applied for and granted within this proposal, Dr. Tiger Jeans was hired as a postdoctoral researcher at the start of the program in September of 2008 to perform the numerical simulations. Dr. Tiger Jeans returned to his homeland of Canada in September of 2009 and started in a permanent position as Defence Scientist for Warship Performance at Defence R&D Canada – Atlantic.

He was followed by Dr. John Imamura, who continues to perform the simulations that are part of this research. He joined the program in May 2010.

In addition, I involved as many USAFA teaching faculty members as possible in the program. This was in part due to intense interest, but also helped greatly in speeding up progress during the time intensive experimental setup portion of this project. The faculty members were sponsoring teams of 2-3 Cadets within the Aeronautics 471 class, where senior cadets participate in ongoing research programs in the Department. This gives the cadets a unique opportunity to perform funded research, an experience that many undergraduate students at typical research universities are missing. The Cadets are assigned a manageable portion of a larger project, and under close mentoring from their faculty sponsor experience all phases of a research project from literature and background research, test plan development, testing to data post processing, data analysis and final report writing and presentation of the results. In the spring semester 2009, a total of three research teams were involved in the cycloidal wave energy converter research program:

- LtCol Brad Thompson, Ph.D., with Cadets Coolis and Ortiz developed and calibrated the two component force balances to be used in the water tunnel model
- LtCol Tim Jung with Cadets Bell and Baker commissioned a new Laser Doppler Velocimetry system and performed wake traverses downstream of the cycloidal turbine
- Cadets Parson, Chronister and Tay worked with the PI on energy extraction in steady flow.

Involvement of other USAFA faculty members during the spring 2009 semester:

- Dipl. Ing. Manfred Meid joined the program as a visiting Engineer from the BWB in Germany through the Engineering and Scientist Exchange Program (ESEP) at no cost to the program. He was working full time on this project since December 2008.
- Dr. Michael Maixner, Engineering Mechanics, joined the team as an expert on potential flow solutions assisting in code development

In the fall semester 2009 as well as the spring semester of 2010, a total of four research teams were involved in the cycloidal wave energy converter research program:

- Casey Fagley, Ph.D. candidate, worked with Cadets Thiago Huxley and Christopher Hartman on a feedback controlled cycloidal wave energy converter in simulated shallow water waves (Fall 09)
- Cadets Matthew D. Roland and Sarah E. Skogsberg worked with the PI on force measurements on the cycloidal wave energy converter blades. (Fall 09)
- Cadets Shelby Judd and Zach White worked with the PI on wake measurements using Laser Doppler Velocimetry (LDV) (Fall 09)

- Casey Fagley, Ph.D. candidate, worked with Cadets Boyd and Weakley on a feedback controlled cycloidal wave energy converter in simulated shallow water waves (Spring 10)
- Cadets Mary Gaudreault and Daniel Wabinga worked with the PI on commissioning of the USAFA Wave Tunnel (Spring 10)

Involvement of other USAFA faculty members during the 2009-2010 grant year:

- Dipl. Ing. Rolf Hellbutsch joined the program as a visiting Engineer from the BWB in Germany through the Engineering and Scientist Exchange Program (ESEP) at no cost to the program. He was working full time on this project since December 2009.
- Dr. Michael Maixner, Engineering Mechanics, continued working with the team as an expert on potential flow solutions assisting in code development

Conclusions

In comparison to the expectations that were communicated to the National Science Foundation in the proposal, the results to date have exceeded the original expectation. In particular, the fact that wave cancellation with more than 99% wave absorption can be achieved was better than hoped for. In addition, other features of the Cycloidal Wave Energy converter are very favorable for the actual implementation of the device, namely the almost constant shaft torque and thus power output for a harmonic wave. We were able to understand the basic flow physics at work, as well as the optimal size of the device along with the range of wave lengths of incoming waves that can be efficiently cancelled. At this point all the data is suggesting that the Cycloidal Wave Energy Converter can be developed into a superior wave energy conversion device that solves the main problems that have prevented wave energy from being used commercially so far, which are efficiency as well as survivability of storms. Even though, major scientific and engineering efforts will be needed for this to become a reality.

References

Publications resulting from this research program

- [1] Siegel, S. G.; Jeans, T. & McLaughlin, T. Intermediate Ocean Wave Termination Using a Cycloidal Wave Energy Converter 29th International Conference on Ocean, Offshore and Arctic Engineering (OMAE), 2010
- [2] Siegel, S. G.; Jeans, T. & McLaughlin, T. Deep Ocean Wave Energy Conversion using a Cycloidal Turbine Applied Ocean Research, 2010, submitted
- [3] Siegel, S.; Jeans, T. & McLaughlin, T. Deep Ocean Wave Cancellation Using a Cycloidal Turbine 62nd Annual Meeting of the American Physical Society, Division of Fluid Dynamics, Minneapolis, MN, 2009
- [4] Skogsberg and Roland, Force measurements on the cycloidal wave energy converter blades. Aeronautics 471 Final Report, Fall 2009
- [5] Huxley and Hartman, A feedback controlled cycloidal wave energy converter in simulated shallow water waves, Aeronautics 471 Final Report, Fall 2009

- [6] Judd and White, Wake measurements in a Cycloidal Wave Energy Converter using Laser Doppler Velocimetry, Aeronautics 471 Final Report, Fall 2009
- [7] Boyd and Weakley, A feedback controlled cycloidal wave energy converter in simulated shallow water waves, Aeronautics 471 Final Report, Spring 2010

Open literature references

- [8] Boyle, G., 'Renewable Energy - Power for a sustainable future', Oxford University Press, 2004
- [9] Bedart, R., 'Final Summary Report - Offshore Wave Power Feasibility Demonstration Project', E2I EPRI Global, WP 009 - US Rev 1, 2005
- [10] Falnes, Johannes, 'Ocean Waves and Oscillating Systems', Cambridge University Press, 2002
- [11] G. M. Darrieus, 'Turbine having its rotating shaft transverse to the flow of the current', U.S. Patent, 1,835,018, 1931
- [12] Kiho, S., Shiono, M., and Suzuki, K., 'The Power Generation from Tidal Currents by Darrieus Turbine', WREC 1996, 1996
- [13] S. McIntosh, H. Babinsky, T. Bertenyi, 'Optimizing the Energy Output of Vertical Axis Wind Turbines for Fluctuating Wind Conditions', 45th AIAA Aerospace Sciences Meeting and Exhibit, Reno, Nevada, AIAA-2007-1368, Jan. 8-11, 2007
- [14] Siegel, Stefan, 'Numerical Unsteady Cyclical Propeller Feasibility Study', Final Report to AFOSR, September 2006
- [15] Siegel, Stefan; Seidel, Jürgen; Cohen, Kelly; McLaughlin, Thomas, 'A Cycloidal Propeller Using Dynamic Lift', 37th AIAA Fluid Dynamics Conference, Miami, FL, 2007
- [16] S.G. Siegel, "Cyclical Wave Energy Converter", U. S. Patent 7,686,583 – 2010 and pending / awarded International Patent applications with priority date May 2006.
- [17] S.G. Siegel, "Vortex Shedding Cyclical Propeller", U. S. Patent 7,762,776 - 2010 and pending / awarded international applications with priority date July 2006.
- [18] Werle, M. J. Wind Turbine Wall Blockage Corrections, *FloDesign Inc. Wilbraham, MA 01095*
- [19] Wehausen, J. & Laitone, E., Surface Waves, Handbook of Physics, Vol.9, *Springer-Verlag*, 1960